



Numerical Relativity Simulations of the Neutron Star Merger GW170817: Long-term Remnant Evolutions, Winds, Remnant Disks, and Nucleosynthesis

Vsevolod Nedora¹, Sebastiano Bernuzzi¹ , David Radice^{2,3,4} , Boris Daszuta¹, Andrea Endrizzi¹, Albino Perego^{5,6} , Aviral Prakash^{2,3}, Mohammadtaher Safarzadeh⁷ , Federico Schianchi¹, and Domenico Logoteta^{8,9}

¹Theoretisch-Physikalisches Institut, Friedrich-Schiller-Universität Jena, D-07743, Jena, Germany

²Institute for Gravitation & the Cosmos, The Pennsylvania State University, University Park, PA 16802, USA

³Department of Physics, The Pennsylvania State University, University Park, PA 16802, USA

⁴Department of Astronomy & Astrophysics, The Pennsylvania State University, University Park, PA 16802, USA

⁵Dipartimento di Fisica, Università di Trento, Via Sommarive 14, I-38123 Trento, Italy

⁶INFN-TIFPA, Trento Institute for Fundamental Physics and Applications, via Sommarive 14, I-38123 Trento, Italy

⁷Center for Astrophysics, Harvard & Smithsonian, 60 Garden Street, Cambridge, MA 02138, USA

⁸Dipartimento di Fisica, Università di Pisa, Largo Pontecorvo 3, I-56127 Pisa, Italy

⁹Istituto Nazionale di Fisica Nucleare (INFN), Largo Pontecorvo 3, I-56127 Pisa, Italy

Received 2020 August 15; revised 2020 November 2; accepted 2020 November 10; published 2021 January 13

Abstract

We present a systematic numerical relativity study of the dynamical ejecta, winds, and nucleosynthesis in neutron star (NS) merger remnants. Binaries with the chirp mass compatible with GW170817, different mass ratios, and five microphysical equations of state (EOSs) are simulated with an approximate neutrino transport and a subgrid model for magnetohydrodynamic turbulence up to 100 ms postmerger. Spiral density waves propagating from the NS remnant to the disk trigger a wind with mass flux $\sim 0.1\text{--}0.5 M_{\odot} \text{ s}^{-1}$, which persists for the entire simulation as long as the remnant does not collapse to a black hole. This wind has average electron fraction $\gtrsim 0.3$ and average velocity $\sim 0.1\text{--}0.17 c$ and thus is a site for the production of weak r -process elements (mass number $A < 195$). Disks around long-lived remnants have masses $\sim 0.1\text{--}0.2 M_{\odot}$, temperatures peaking at $\lesssim 10$ MeV near the inner edge, and a characteristic double-peak distribution in entropy resulting from shocks propagating through the disk. The dynamical and spiral-wave ejecta computed in our targeted simulations are not compatible with those inferred from AT2017gfo using two-components kilonova models. Rather, they indicate that multicomponent kilonova models including disk winds are necessary to interpret AT2017gfo. The nucleosynthesis in the combined dynamical ejecta and spiral-wave wind in the long-lived mergers of comparable mass robustly accounts for all the r -process peaks, from mass number ~ 75 to actinides in terms of solar abundances. Total abundances are weakly dependent on the EOS, while the mass ratio affects the production of first-peak elements.

Unified Astronomy Thesaurus concepts: Gravitational waves (678); Gravitational wave astronomy (675); Nucleosynthesis (1131); R-process (1324)

1. Introduction

The mass ejection of neutron-rich matter from binary neutron star (BNS) mergers has been studied theoretically since the 1970s as a possible site for r -process nucleosynthesis (Lattimer & Schramm 1974; Symbolist & Schramm 1982; Freiburghaus et al. 1999; Rosswog et al. 1999; Rosswog 2005). The radioactive decay of r -process elements produces a characteristic electromagnetic (EM) transient in the UV/optical/near-IR bands, called a kilonova (kN) (Li & Paczynski 1998; Kulkarni 2005; Metzger et al. 2010; Roberts et al. 2011; Kasen et al. 2013), which was observed as a counterpart of the gravitational-wave (GW) event GW170817 (Abbott et al. 2017a, 2017b, 2019a, 2019b) and named AT2017gfo (Arcavi et al. 2017; Coulter et al. 2017; Drout et al. 2017; Evans et al. 2017; Hallinan et al. 2017; Kasliwal et al. 2017; Nicholl et al. 2017; Smartt et al. 2017; Soares-Santos et al. 2017; Tanvir et al. 2017; Troja et al. 2017; Mooley et al. 2018; Ruan et al. 2018; Lyman et al. 2018). The near-IR luminosity of AT2017gfo peaked several days after the merger (Chornock et al. 2017), and this is consistent with the expectation that the opacities of expanding r -process material are dominated by lanthanides and possibly actinides (Kasen et al. 2013). The UV/optical luminosity peaked instead less than one day after the merger (Nicholl et al. 2017), and it originates from ejected material that experienced only a partial r -process nucleosynthesis (Martin et al. 2015).

The ejecta masses inferred from observations (Cowperthwaite et al. 2017; Perego et al. 2017; Tanaka et al. 2017; Tanvir et al. 2017; Villar et al. 2017; Kawaguchi et al. 2018) are not compatible with those predicted by numerical simulations with targeted neutron star (NS) masses, and several questions remain open. In particular, the early blue kN remains a challenging aspect to explain for most models. Both semi-analytical and radiation transport models require large ejecta velocities and electron fractions (Y_e), different from those found in simulations (e.g., Fahlman & Fernández 2018; Nedora et al. 2019). The late red kN component requires ejecta masses generally not observed for the dynamical ejecta computed in numerical relativity (NR) simulations (Radice et al. 2018b). In addition, the number of components and the geometry of the emission can have a significant effect on the ejecta parameters (Perego et al. 2017; Kawaguchi et al. 2018). Also, it is important to note that the diffusion and emission of photons are often simplified in semi-analytical kN models (e.g., Perego et al. 2017; Villar et al. 2017; Siegel 2019), and more accurate radiation transfer computations may alter the inferred ejecta parameters (Kawaguchi et al. 2018; Korobkin et al. 2020). However, simulations of photon radiation transfer often employ ad hoc, simplified ejecta different from those computed from ab initio simulations.

Key for interpreting BNS electromagnetic emissions is the detailed modeling of the mass ejection from BNS mergers,

which must include general relativity, a microphysical equation of states (EOS) of strongly interacting matter, relativistic (magneto)hydrodynamics, and neutrino transport. NR simulations performed so far mostly focused on the dynamical ejecta that are launched during a merger by tidal torques (tidal component) and by the shocks generated by the bounce of the NS cores (shocked component) (e.g., Hotokezaka et al. 2013; Bauswein et al. 2013; Wanajo et al. 2014; Sekiguchi et al. 2015, 2016; Radice et al. 2016b, 2018b; Vincent et al. 2020). In equal-mass mergers, the shocked component is found to be a factor ~ 10 more massive than the tidal component. This is in contrast to early works that employed Newtonian gravity and in which the tidal component dominated the ejecta due to the weaker gravity and stiffer EOS employed in those simulations (Ruffert et al. 1997; Rosswog et al. 1999, 2003, 2014; Rosswog & Davies 2003; Rosswog & Liebendoerfer 2003; Rosswog & Ramirez-Ruiz 2003; Oechslin et al. 2006; Korobkin et al. 2012). However, even the dynamical ejecta found in NR simulations cannot account alone for the bright blue and late red components of the observed kN in AT2017gfo (Siegel 2019).

Winds originating from the merger remnant on timescales of $\mathcal{O}(0.1\text{--}1)$ s can unbind $\mathcal{O}(0.1) M_\odot$ from the remnant and represent (if present) the largest contribution to the kilonova signal (Dessart et al. 2009; Fernández et al. 2015, 2019; Just et al. 2015; Lippuner et al. 2017; Siegel & Metzger 2017; Fujibayashi et al. 2018, 2020a; Radice et al. 2018a; Janiuk 2019; Miller et al. 2019; Mösta et al. 2020). Thus far, these winds have been mostly studied by means of long-term Newtonian simulations of neutrino-cooled disks, assuming simplified initial conditions (e.g., Beloborodov 2008; Metzger et al. 2008; Lee et al. 2009; Fernández & Metzger 2013). Ab initio (3+1)D NR simulations of the merger with weak interactions and magnetohydrodynamics are not yet fully developed at sufficiently long timescales (Sekiguchi et al. 2011, 2015, 2016; Wanajo et al. 2014; Palenzuela et al. 2015; Radice et al. 2016b, 2018a; Lehner et al. 2016a; Foucart et al. 2017; Bovard et al. 2017; Fujibayashi et al. 2018, 2017; Nedora et al. 2019; Bernuzzi et al. 2020; Vincent et al. 2020). These simulations are essential to interpret AT2017gfo and future events. For example, long-term (up to 100 ms postmerger) NR simulations pointed out the existence of spiral-wave wind in which there are favourable conditions (large ejecta mass, high velocity, and not extremely neutron-rich conditions) for the early emission from lanthanide-poor material (Nedora et al. 2019). Such mass ejection can also be boosted by global large-scale magnetic stresses (Metzger et al. 2018; Siegel & Metzger 2018, 2017), although significant mass fluxes can only be achieved by fine-tuning the initial configuration or setting an unrealistic strength of the magnetic field (e.g., Ciolfi 2020; Mösta et al. 2020). A third contribution can come from neutrino-driven winds of mass $\sim 10^{-4}\text{--}10^{-3} M_\odot$ originating above the remnant, but their mass cannot account for bright signals (Dessart et al. 2009; Perego et al. 2014; Just et al. 2015).

The nucleosynthesis from BNS mergers is believed to provide a major contribution to the r -process material in the universe. However, whether or not BNS mergers are the only source is still debated, and possible additional r -process sites, such as collapsars, jet-driven supernovae, and NS implosions, have been proposed (Argast et al. 2004; Duan et al. 2011; Winteler et al. 2012; Hirai et al. 2015; Nishimura et al. 2015, 2017; Bramante & Linden 2016; Fuller et al. 2017; Mösta et al. 2018; Siegel et al. 2018; Bartos & Marka 2019; Ji et al. 2019; Wehmeyer et al. 2019;

van de Voort et al. 2020; Vassh et al. 2020). In particular, it is not clear whether BNS mergers can explain r -process enriched ultrafaint dwarf galaxies, classical dwarf galaxies (Bramante & Linden 2016; Ji et al. 2016; Safarzadeh et al. 2019a, 2019b; Bonetti et al. 2019; Skúladóttir et al. 2019), and the evolution of r -process abundances at both early and late times (Safarzadeh & Côté 2017; Bonetti et al. 2018; Safarzadeh et al. 2019b; Hotokezaka et al. 2018; Côté et al. 2019; Banerjee et al. 2020).

In this work we address the problem of the remnant evolution on the viscous timescale by means of ab initio (3+1)D NR simulations. We present new simulations performed with five microphysical EOSs, an M0 neutrino transport scheme and a subgrid model for the magnetohydrodynamic turbulence. We compute dynamical ejecta and spiral-wave wind, and we calculate the nucleosynthesis of the resulting unbound mass. The simulations and analysis methods are detailed in Section 2. Section 3 gives an overview of the remnant dynamics, describing the main features in terms of the binary parameters. The properties of the dynamical ejecta are summarized in Section 4, where we compare with simple models used for AT2017gfo. Sections 5 and 6 describe the mechanism powering the spiral-wave wind and ν -component in long-lived remnants. This mechanism is a combination of $m = 2$ and $m = 1$ modes in the remnant powering spiral density waves in the disk. A polar component of the spiral-wave wind is powered by neutrino heating above the remnant. The properties of the remnant disk, including thermodynamical quantities, are discussed in Section 7. The composition of the disk at the end of the simulations is characterized by double peaks in the profiles of entropy and electron fraction. Section 8 presents nucleosynthesis calculations on the combined dynamical and wind ejecta. The combined yields in the ejecta of long-lived remnants show a good fit to the solar abundance patterns for all r -process peaks. Throughout the text we discuss the implications of our results for AT2017gfo.

2. Methods

Within (3+1)D NR we solve the equations of general relativistic hydrodynamics for a perfect fluid coupled to the Z4c free evolution scheme for Einstein's equations (Bernuzzi & Hilditch 2010; Hilditch et al. 2013). The interactions between the neutrino radiation and the fluid are treated with a leakage scheme in the optically thick regions (Ruffert et al. 1996; Galeazzi et al. 2013; Neilsen et al. 2014) while free-streaming neutrinos are evolved according to the M0 scheme (Radice et al. 2018b). The effects of large-scale magnetic fields are simulated with the method of general relativistic large-eddy simulations (GRLES) for turbulent viscosity (Radice 2017).

2.1. Matter and Radiation Treatment

We write the fluid's stress-energy tensor as

$$T_{\mu\nu} = \rho h u_\mu u_\nu + P g_{\mu\nu} \quad (1)$$

where $\rho = m_b n$ is the baryon rest-mass density, n the baryon number density, $m_b \simeq 10^{-24}$ g the neutron mass, $h = 1 + \epsilon + P/\rho$ the specific enthalpy, ϵ the specific internal energy, u^μ the fluid 4-velocity, and P the pressure. The fluid satisfies Euler's equations:

$$\nabla_\nu T^{\mu\nu} = Q u^\mu, \quad (2)$$

where Q is the net energy exchange rate due to the absorption and emission of neutrinos, given by Equation (11) of

Table 1
Weak Reactions Employed in Our Simulations and References for Their Implementation

Reaction	Role	References
$p + e^- \leftrightarrow \nu_e + n$	P, A	Bruenn (1985)
$n + e^+ \leftrightarrow \bar{\nu}_e + p$	P, A	Bruenn (1985)
$e^+ + e^- \rightarrow \nu + \bar{\nu}$	P	Ruffert et al. (1996)
$\gamma + \gamma \rightarrow \nu + \bar{\nu}$	P	Ruffert et al. (1996)
$N + N \rightarrow \nu + \bar{\nu} + N + N$	P	Burrows et al. (2006)
$\nu + N \rightarrow \nu + N$	S	Ruffert et al. (1996)
$\nu + A \rightarrow \nu + A$	S	Shapiro & Teukolsky (1983)

Note. In the left column, $\nu \in \{\nu_e, \bar{\nu}_e, \nu_x\}$ denotes any neutrino species, ν_x any heavy-lepton neutrinos, $N \in \{n, p\}$ a nucleon, and A any nucleus. In the central column the role of each reaction is highlighted, with “P” standing for production, “A” for absorption opacity, and “S” for scattering opacity. When two roles are indicated, the second refers to the inverse (\leftrightarrow) reaction.

Radice et al. (2018b). The above system of equations is closed by a finite-temperature (T), composition-dependent EOS in the form $P = P(\rho, Y_e, T)$ and by the evolution equations for the proton and neutron number densities:

$$\nabla_\nu(n_p u^\mu) = R_p^\mu, \quad \nabla_\nu(n_n u^\mu) = R_n^\mu. \quad (3)$$

where the total proton fraction is computed as $n_p = Y_e n$, $n_p + n_n = n$, and $R_p = -R_n$ is the net lepton number exchange rate due to the absorption and emission of neutrinos and antineutrinos.

We treat compositional and energy changes in the material due to weak reactions using the leakage scheme presented in Galeazzi et al. (2013) and Radice et al. (2016b); see also van Riper & Lattimer (1981), Ruffert et al. (1996), Rosswog & Liebendoerfer (2003), O’Connor & Ott (2010), Sekiguchi (2010), Neilsen et al. (2014), Perego et al. (2016), Ardevol-Pulpillo et al. (2019), and Gizzi et al. (2019) for other implementations. We track reactions involving electron neutrinos (ν_e) and antineutrinos ($\bar{\nu}_e$) separately, and treat heavy-lepton neutrinos in a single effective species (ν_x). The production rates R_ν , $\nu \in \{\nu_e, \bar{\nu}_e, \nu_x\}$, the associated production energies Q_ν , and neutrino absorption opacity $\kappa_{\nu,a}$ and scattering opacity $\kappa_{\nu,s}$ are computed from the reactions listed in Table 1. Charged-current weak reactions on nucleons produce ν_e ’s and $\bar{\nu}_e$ ’s, and provide absorption opacity for them. The production of neutrino pairs of all flavors, and in particular of ν_x pairs, is supplied by thermal processes (including electron–positron annihilation and plasmon decay) and nucleon–nucleon bremsstrahlung. Quasielastic scattering off nucleons is the major source of scattering opacity for all neutrino species, while we neglect the subdominant absorption processes involving heavy flavor neutrinos. According to the resulting diffusion optical depth, neutrinos are then split into a trapped component with number density n_ν^{trap} and a free-streaming component n_ν^{fs} . The latter are emitted according to the effective rate R_ν^{eff} (Ruffert et al. 1996) (see Radice et al. 2018b, Equation (4)) and with average energy $Q_\nu^{\text{eff}}/R_\nu^{\text{eff}}$ and then evolved according to the M0 scheme of Radice et al. (2018b). The M0 scheme evolves the number density of the free-streaming neutrinos assuming that they move along radial null rays, and estimates the free-streaming neutrino energy, E_ν , under the additional assumption of a stationary metric. Note that the pressure due to the trapped neutrino component is neglected, since it is found to be important at a level $\lesssim 5\%$ in the

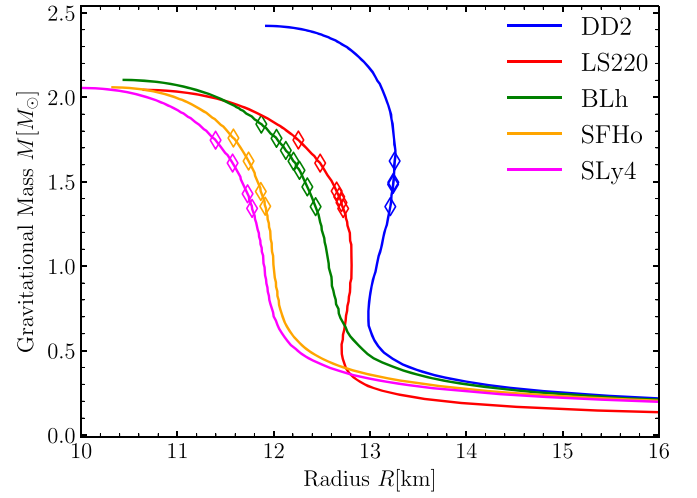


Figure 1. Mass–radius relations for the EOSs used in this work. Markers along the sequences indicate the NSs simulated in this work.

conditions relevant for BNS mergers (Galeazzi et al. 2013; Perego et al. 2019).

Our simulations do not include magnetic fields but we simulate the angular momentum transport due to magneto-hydrodynamic turbulence by using an effective viscosity and the GRLES scheme (Radice 2017, 2020). The subgrid model employed in this work is described in Radice (2020), and it is designed based on the results of the high-resolution general relativistic magnetohydrodynamic simulations of a BNS merger of Kiuchi et al. (2018). This GRLES subgrid model has been already used in Perego et al. (2019), Endrizzi et al. (2020), Nedora et al. (2019), and Bernuzzi et al. (2020).

2.2. EOS Models

We consider five different nuclear EOS models: BLh, DD2, LS220, SFHo, and SLy4 (see Perego et al. 2019, Table 1) where DD2, LS220, and SFHo are summarized). All these EOSs include neutrons (n), protons (p), nuclei, electrons, positrons, and photons as relevant degrees of freedom. Cold, neutrino-less β -equilibrated matter described by these microphysical EOSs predicts NS maximum masses and radii within the range allowed by current astrophysical constraints, including the recent GW constraint on tidal deformability (Abbott 2017c, 2018, 2019b; De et al. 2018). The mass–radius diagram with these EOSs is shown in Figure 1. All EOS models have symmetry energies at saturation density within experimental bounds. However, LS220 has a significantly steeper density dependence of its symmetry energy than the other models (Lattimer & Lim 2013; Danielewicz & Lee 2014), and it could possibly underestimate the symmetry energy below saturation density. In the considered models thermal effects enter in a quite different way. In particular particle correlations beyond the mean-field approximation are included only in the BLh EOS. Such effects play an important role in the thermal evolution of NS matter. In the other models these effects are mainly encoded in the nucleon effective mass, which depends on density and temperature. At fixed entropy, the smaller the effective mass, the higher the temperature.

The BLh EOS is a new finite-temperature EOS derived in the framework of the non-relativistic many-body Brueckner–Hartree–Fock (BHF) approach (D. Logoteta et al. 2020, in preparation). The zero-temperature, β -equilibrated version of this EOS was first presented in Bombaci & Logoteta (2018)

and applied to BNS mergers in Endrizzi et al. (2018); the finite-temperature extension was employed in Bernuzzi et al. (2020), where a more detailed description can be found. The interactions between nucleons are described through a potential derived perturbatively in chiral effective field theory (Machleidt & Entem 2011). It consists of a two-body part (Piarulli et al. 2016) calculated up to next to next to next-to-leading (N3LO) order and three-nucleon interaction calculated up to N2LO (Logoteta et al. 2016). At low densities ($n \lesssim 0.05 \text{ fm}^{-3}$) it is smoothly connected to the SFHo EOS (Bernuzzi et al. 2020).

The DD2 and the SFHo EOSs are based on relativistic mean-field (RMF) theory of high-density nuclear matter (Typel et al. 2010; Hempel & Schaffner-Bielich 2010). Both the EOSs contain neutrons, protons, light nuclei such as deuterons, helions, tritons, and alpha particles, and heavy nuclei in nuclear statistical equilibrium (Steiner et al. 2013b). DD2 and SFHo use different parameterizations of the covariant Lagrangian that models the mean-field nuclear interactions. The resulting RMF equations are solved in Hartree’s approximation. In particular, DD2 uses linear, but density-dependent coupling constants (Typel et al. 2010), while the RMF parameterization of SFHo employs constant couplings adjusted to reproduce measurements of NS radius from low-mass X-ray binaries (see Steiner et al. 2013a and references therein). The DD2 is the stiffest EOS model considered in the present work and it is not in very good agreement with the so-called flow-constraint (Danielewicz et al. 2002).

The LS220 (Lattimer & Swesty 1991) and the SLy4 EOSs are based on a liquid droplet model of Skyrme interaction. The LS220 EOS includes surface effects and models α -particles as an ideal, classical, non-relativistic gas. Heavy nuclei are treated using the single-nucleus approximation (SNA). LS220 does not satisfy the constraints from chiral effective field theory (Hempel et al. 2017). The SLy4 Skyrme parameterization was originally introduced in Douchin & Haensel (2001) for cold nuclear and NS matter. In this work we employ the finite-temperature extension presented in Schneider et al. (2017) using an improved version of the LS220 model that includes non-local isospin asymmetric terms. In this EOS version a better and more consistent treatment of both nuclear surface properties and the size of heavy nuclei is also introduced.

2.3. Computational Setup

We prepare irrotational BNS initial data in quasi-circular orbit with NSs at an initial separation of 45 km, corresponding to ~ 3 –4 orbits before merger. Initial data are computed using the `Lorene` multidomain pseudospectral library (Gourgoulhon et al. 2001). The EOS used for the initial data is constructed from the minimum-temperature slice of the EOS table used for the evolution assuming neutrino-less β -equilibrium.

Initial data are evolved with the `WhiskyTHC` code (Radice & Rezzolla 2012; Radice et al. 2014a, 2014b) for general relativistic hydrodynamics that implements the approximate neutrino transport scheme developed in Radice et al. (2016b, 2018b) and the GRLES for turbulent viscosity (Radice 2017) described above. The M0 scheme is switched on shortly before the two NSs collide, when neutrino matter interactions become dynamically important. The equations for the M0 scheme are solved on a uniform spherical grid extending to $\simeq 756$ km and having $n_r \times n_\theta \times n_\phi = 3096 \times 32 \times 64$ grid points.

`WhiskyTHC` is implemented within the `Cactus` framework (Goodale et al. 2003; Schnetter et al. 2007) and coupled to an adaptive mesh refinement (AMR) driver and a metric solver. The Z4c spacetime solver is implemented in the `CTGamma` code (Pollney et al. 2011; Reisswig et al. 2013b), which is a part of the `Einstein Toolkit` (Löffler et al. 2012). We use fourth-order finite-differencing for the metric’s spatial derivatives and the method of lines for the time evolution of both metric and fluid variables. We adopt the optimal, strongly stability-preserving third-order Runge–Kutta scheme (Gottlieb et al. 2009) as time integrator. The time step is set according to the speed-of-light Courant–Friedrich–Lewy (CFL) condition with CFL factor 0.15. While numerical stability requires the CFL to be less than 0.25, the smaller value of 0.15 is necessary to guarantee the positivity of the density when using the positivity-preserving limiter implemented in `WhiskyTHC`.

The computational domain is a cube of 3024 km in side length whose center is at the center of mass of the binary. Our code uses Berger–Olinger conservative AMR (Berger & Olinger 1984) with sub-cycling in time and refluxing (Berger & Colella 1989; Reisswig et al. 2013a) as provided by the `Carpet` module of the `Einstein Toolkit` (Schnetter et al. 2004). We set up an AMR grid structure with seven refinement levels. The finest refinement level covers both NSs during the inspiral and the remnant after the merger, and has a typical resolution of $h \simeq 246$ m (grid setup named LR), $h \simeq 185$ m (SR), or $h \simeq 123$ m (HR). The computational cost of these simulations is more than 40M CPU-hours.

2.4. Postprocess Analysis

To study the dynamical modes in the remnant we follow previous work (Paschalidis et al. 2015; East et al. 2016a; Radice et al. 2016a) and define a complex azimuthal mode decomposition of the rest-mass density as

$$C_m = \int \rho W e^{-im\phi} \sqrt{\gamma} dx dy, \quad (4)$$

where γ is the determinant of the three-metric and W is the Lorentz factor between the fluid and the Eulerian observers. Note that the above quantities are gauge-dependent.

Following a common convention, we define the remnant disk as the baryon material either outside the apparent horizon of the black hole (BH) or with a rest-mass density $\rho \lesssim 10^{13} \text{ g cm}^{-3}$ around an NS remnant. The baryonic mass of the disks is computed as the volume integral of the conserved rest-mass density $D = \sqrt{\gamma} W \rho$ from 3D snapshots of the simulations in postprocessing. The threshold $\rho \sim 10^{13} \text{ g cm}^{-3}$ corresponds to the point in the remnant where the angular velocity profiles becomes approximately Keplerian (e.g., Shibata et al. 2005; Shibata & Taniguchi 2006; Hanauske et al. 2017; Kastaun et al. 2017).

We make use of mass-averaged quantities, and for a quantity f they are computed as

$$\langle f \rangle = \frac{\sum_i f(m_i) m_i}{\sum_i m_i} \quad (5)$$

where m_i is the mass contained in the i th bin.

Analysis of the fluid’s angular momentum in the remnant and disk is performed assuming axisymmetry. That is, we assume $\phi^\mu = (\partial_\phi)^\mu$ to be a Killing vector. Accordingly, the

conservation law

$$\partial_t(T^{\mu\nu}\phi_\nu n_\nu \sqrt{\gamma}) - \partial_i(\alpha T^{i\nu}\phi_\nu \sqrt{\gamma}) = 0, \quad (6)$$

where n^μ is the normal vector to the spacelike hypersurfaces of the spacetime's 3+1 decomposition, implies the conservation of the angular momentum

$$J = -\int T_{\mu\nu} n^\mu \phi^\nu \sqrt{\gamma} d^3x. \quad (7)$$

In the cylindrical coordinates $x^i = (r, \phi, z)$ adapted to the symmetry the angular momentum density is

$$j = \rho h W^2 v_\phi, \quad (8)$$

and the angular momentum flux is

$$\alpha \sqrt{\gamma} T_\nu^r \phi^\nu = \alpha \sqrt{\gamma} \rho h W^2 (v^r v_\phi). \quad (9)$$

All considered mass ejecta are calculated on a coordinate sphere at $R \simeq 294$ km. The dynamical ejecta is computed assuming the fluid elements to follow unbound geodesics, $-u_t > 1$, and to reach an asymptotic velocity $v_\infty \simeq \sqrt{2E_\infty} = \sqrt{1 - u_t^2}$. Wind ejecta are instead computed according to the Bernoulli criterion $-hu_t > 1$, and the associated asymptotic velocity is calculated as $v_\infty \simeq \sqrt{2h(E_\infty + 1) - 1}$. Note that the geodesic criterion above neglects the fluid's pressure and might underestimate the ejecta mass. The Bernoulli criterion assumes that the (test fluid) flow is stationary, so that there is a pressure gradient that can further push the ejecta. We find that both criteria predict dynamical ejecta masses that are practically indistinguishable and well within the numerical uncertainties (Bernuzzi et al. 2020) if applied to extraction spheres at large coordinate radii; differences between the two criteria are instead present if they are applied to matter volumes (see Kastaun & Galeazzi 2015).

2.5. Simulations

We discuss simulations of 37 binaries with chirp mass $M_c = 1.188 M_\odot$ compatible with the source of GW170817, total gravitational mass spanning the range $M \in [2.73, 2.88] M_\odot$ and mass ratio values $q = M_A/M_B \in [1, 1.8]$. The masses and radii of the NSs in the simulated binaries are shown as markers in the mass-radius diagram of Figure 1. Summary data for the simulations are collected in Table 2. Most of the binaries are simulated at both grid resolutions LR and SR, and 16 binaries are simulated also at HR for a total of 76 simulations. We follow the evolution of long-lived remnants up to ~ 100 ms postmerger. Note that a subset of simulations are performed without the GRLES scheme in order to assess the effect of turbulent viscosity; they are indicated with “*” in the following. The short-term evolution of the binaries with the largest mass ratio has already been presented in Bernuzzi et al. (2020). Together with our previous data these simulations form the largest sample of merger simulations with microphysics available to date (Bernuzzi et al. 2016, 2020; Radice et al. 2016b, 2017, 2018a, 2018b, 2018c; Perego et al. 2019; Endrizzi et al. 2020).

3. Overview of the Remnant Dynamics

The early (dynamical) postmerger phase is driven by the GW emission, which removes about twice as much energy as the whole inspiral-to-merger phase in ~ 10 – 20 ms (Bernuzzi et al. 2016). After this GW postmerger transient at kilohertz frequencies, the GW emission drops significantly and removes angular

momentum only on timescales of a few seconds (Radice et al. 2018a). The remnant evolution on timescales $\mathcal{O}(100)$ ms is then driven by viscous and weak interactions. Merger remnants after the GW-driven phase have a significant excess of angular momentum and gravitational mass if compared to zero-temperature rigidly rotating equilibrium with the same baryonic mass (Radice et al. 2018a). Temperature and composition effects are key to determine whether the remnant evolves toward an axisymmetric stationary NS close to the mass-shedding or collapses to a BH. The new simulations presented here allow us to investigate these timescales with the relevant physical effects.

The short-term dynamics of 10 of these BNSs have been previously discussed in Bernuzzi et al. (2020), in the context of prompt collapse of binaries with large mass ratio.¹⁰ Indeed, the only merger remnants that promptly collapse in the simulated sample are those with $q \gtrsim 1.67$. The collapse in the mergers of BLh, LS220, SFHo, and SLy with $q = 1.67$ and 1.8 is induced by the accretion of the (less massive) companion onto the primary NS. In these cases, the BH remnant is surrounded by an accretion disk formed by the tidal tail of the companion. The disk is thus composed of very neutron-rich material with $Y_e \sim 0.1$ and with baryon masses at formation $\sim 0.15 M_\odot$, significantly heavier than the remnant disks in prompt collapse mergers of equal masses. Examples of the evolution of disk mass are shown in Figure 2 for representative BNSs. These high- q mergers launch dynamical ejecta of mass $\sim 0.01 M_\odot$ that also originate from the tidal disruption of the companion. The dynamical ejecta are neutron-rich and expand from the orbital plane with a crescent-like geometry different from the more isotropic dynamical ejecta of the equal-mass mergers (Bernuzzi et al. 2020).

Among the mergers of comparable mass ($q \lesssim 1.4$), the merger outcome is either a short-lived or a long-lived NS remnant. The former collapses to a BH within few dynamical periods set by the NS remnant's rotation; the latter does not collapse within the simulated time. In practice, the short-lived remnants of LS220 $q = 1, 1.1, 1.2$, SFHo $q = 1, 1.1, 1.4$, and SLy $q = 1, 1.1, 1.4$ collapse within 20 ms postmerger. The exact time of the collapse is strongly dependent on the simulated physics and also on numerical errors. For example, the inclusion of turbulent viscosity (Radice 2017) or changes in the resolution can accelerate or delay the collapse.

The remnant disk originates from the matter expelled by tidal torques and shocks produced at the collisional interface of the NS cores during merger. Starting at merger, the NS remnant sheds mass and angular momentum outward through spiral density waves streaming from the shock interface (Bernuzzi et al. 2016; Radice et al. 2018a). The maximum temperatures are experienced in these streams; they rapidly decrease because of the fluid's expansion and neutrino emission. The electron fraction is reset by an initial excess of electron antineutrino emission and electron neutrino absorption, while the entropy per baryon varies between 3 and $\lesssim 10 k_B/\text{baryon}$ (Perego et al. 2019). In the short-lived cases, the process quickly shuts down at BH formation: the disk rapidly accretes at early times around the newly formed BH and then reaches a steady state, Figure 2. The resulting configuration is approximately axisymmetric and Keplerian; it is characterized by neutron-rich, $Y_e \sim 0.1$, and hot $T \sim 10$ MeV material in the inner part ($\rho \sim 10^{13}$ g cm $^{-3}$) and

¹⁰ Here prompt collapse refers to those mergers in which the central density increases monotonically and there is no core bounce (Bernuzzi 2020; Bernuzzi et al. 2020; Radice et al. 2020).

Table 2
Summary Table of All the Simulations and Dynamical Ejecta Properties

EOS	q	$\tilde{\Lambda}$	Resolution	GRLES	t_{end} (ms)	t_{BH} (ms)	t_{disk} (ms)	$M_{\text{disk}}^{\text{last}}$	M_{ej}^{d} ($10^{-2} M_{\odot}$)	$\langle Y_e^{\text{d}} \rangle$	$\langle v_{\infty}^{\text{d}} \rangle$ (c)	$\langle \theta_{\text{ej}}^{\text{d}} \rangle$ (deg)
BLh	1.00	541	LR SR HR	✓	43.3 91.8 23.1	>43.3 >91.8 >23.1	23.1	$0.166^{+0.052}_{-0.052}$	$0.14^{+0.02}_{-0.02}$	$0.27^{+0.01}_{-0.01}$	$0.17^{+0.01}_{-0.01}$	$39.65^{+0.35}_{-0.35}$
BLh	1.00	541	LR SR	X	15.9 103.2	>15.9 >103.2	15.6	$0.261^{+0.008}_{-0.008}$	$0.12^{+0.01}_{-0.01}$	$0.27^{+0.01}_{-0.01}$	$0.16^{+0.01}_{-0.01}$	$38.80^{+0.44}_{-0.44}$
BLh	1.18	539	LR	✓	69.4	>69.4	69.0	$0.202^{+0.101}_{-0.101}$	$0.30^{+0.06}_{-0.06}$	$0.18^{+0.04}_{-0.04}$	$0.19^{+0.04}_{-0.04}$	$33.65^{+6.73}_{-6.73}$
BLh	1.18	539	LR	X	16.4	>16.4	15.9	$0.229^{+0.115}_{-0.115}$	$0.25^{+0.05}_{-0.05}$	$0.16^{+0.03}_{-0.03}$	$0.20^{+0.04}_{-0.04}$	$30.86^{+6.17}_{-6.17}$
BLh	1.34	539	LR SR	✓	63.4 9.8	>63.4 >9.8	9.8	$0.192^{+0.004}_{-0.004}$	$0.25^{+0.05}_{-0.05}$	$0.14^{+0.04}_{-0.04}$	$0.17^{+0.00}_{-0.00}$	$28.79^{+5.00}_{-5.00}$
BLh	1.34	539	LR	X	18.0	>18.0	18.0	$0.211^{+0.106}_{-0.106}$	$0.19^{+0.04}_{-0.04}$	$0.17^{+0.03}_{-0.03}$	$0.17^{+0.03}_{-0.03}$	$33.39^{+6.68}_{-6.68}$
BLh	1.43	540	LR SR	✓	35.1 59.6	>35.1 >59.6	33.8	$0.265^{+0.001}_{-0.001}$	$0.27^{+0.08}_{-0.08}$	$0.19^{+0.03}_{-0.03}$	$0.16^{+0.00}_{-0.00}$	$34.49^{+3.59}_{-3.59}$
BLh	1.54	543	LR	✓	45.8	>45.8	53.8	$0.324^{+0.162}_{-0.162}$	$0.20^{+0.04}_{-0.04}$	$0.17^{+0.03}_{-0.03}$	$0.13^{+0.03}_{-0.03}$	$31.21^{+6.24}_{-6.24}$
BLh	1.54	543	LR	X	17.4	>17.4	30.1	$0.287^{+0.144}_{-0.144}$	$0.22^{+0.04}_{-0.04}$	$0.21^{+0.04}_{-0.04}$	$0.16^{+0.03}_{-0.03}$	$35.05^{+7.01}_{-7.01}$
BLh	1.66	538	LR SR	✓	64.6 20.1	>64.6 1.8	19.2	$0.289^{+0.005}_{-0.005}$	$0.42^{+0.05}_{-0.05}$	$0.11^{+0.01}_{-0.01}$	$0.12^{+0.01}_{-0.01}$	$24.08^{+0.29}_{-0.29}$
BLh	1.82	532	LR SR HR	✓	12.0 17.5 9.6	1.4 1.4 1.5	5.9	$0.170^{+0.001}_{-0.001}$	$0.81^{+0.04}_{-0.04}$	$0.03^{+0.01}_{-0.01}$	$0.11^{+0.00}_{-0.00}$	$6.53^{+0.65}_{-0.65}$
BLh	1.82	532	LR SR HR	X	53.8 26.3 45.2	1.7 1.3 1.0	43.2	$0.098^{+0.049}_{-0.049}$	$1.07^{+0.07}_{-0.07}$	$0.03^{+0.01}_{-0.01}$	$0.12^{+0.00}_{-0.00}$	$6.27^{+0.53}_{-0.53}$
DD2	1.00	853	LR SR	X	92.0 110.2	>92.0 >110.2	9.4	$0.154^{+0.052}_{-0.052}$	$0.11^{+0.01}_{-0.01}$	$0.25^{+0.00}_{-0.00}$	$0.18^{+0.01}_{-0.01}$	$38.07^{+0.52}_{-0.52}$
DD2	1.00	853	LR SR HR	✓	123.0 113.0 74.4	>123.0 >113.0 >74.4	8.2	$0.111^{+0.040}_{-0.040}$	$0.12^{+0.03}_{-0.03}$	$0.27^{+0.01}_{-0.01}$	$0.16^{+0.00}_{-0.00}$	$40.03^{+0.71}_{-0.71}$
DD2	1.20	847	LR SR HR	X	37.3 91.0 55.2	>37.3 >91.0 >55.2	36.6	$0.261^{+0.028}_{-0.028}$	$0.21^{+0.08}_{-0.08}$	$0.18^{+0.03}_{-0.03}$	$0.17^{+0.01}_{-0.01}$	$29.07^{+3.75}_{-3.75}$
DD2	1.22	847	LR SR HR	✓	42.7 107.3 19.8	>42.7 >107.3 >19.8	8.7	$0.209^{+0.033}_{-0.033}$	$0.25^{+0.02}_{-0.02}$	$0.19^{+0.01}_{-0.01}$	$0.17^{+0.01}_{-0.01}$	$30.74^{+0.89}_{-0.89}$
DD2	1.43	820	LR SR	✓	37.7 62.0	>37.7 >62.0	36.7	$0.304^{+0.051}_{-0.051}$	$0.70^{+0.64}_{-0.64}$	$0.14^{+0.05}_{-0.05}$	$0.14^{+0.01}_{-0.01}$	$25.51^{+9.58}_{-9.58}$
LS220	1.00	715	LR SR	✓	27.0 27.1	13.7 13.7	16.1	$0.073^{+0.032}_{-0.032}$	$0.16^{+0.02}_{-0.02}$	$0.25^{+0.02}_{-0.02}$	$0.16^{+0.01}_{-0.01}$	$35.70^{+0.78}_{-0.78}$
LS220	1.00	715	LR SR HR	X	35.9 37.2 27.1	33.4 16.1 15.4	34.6	$0.072^{+0.006}_{-0.006}$	$0.16^{+0.06}_{-0.06}$	$0.22^{+0.00}_{-0.00}$	$0.16^{+0.01}_{-0.01}$	$34.99^{+1.68}_{-1.68}$
LS220	1.05	715	SR HR	X	23.3 24.1	17.3 13.9	22.3	$0.107^{+0.054}_{-0.054}$	$0.16^{+0.02}_{-0.02}$	$0.21^{+0.01}_{-0.01}$	$0.16^{+0.01}_{-0.01}$	$33.28^{+2.37}_{-2.37}$
LS220	1.11	717	SR HR	X	25.1 24.4	17.0 >24.4	24.2	$0.140^{+0.071}_{-0.071}$	$0.22^{+0.03}_{-0.03}$	$0.19^{+0.02}_{-0.02}$	$0.18^{+0.02}_{-0.02}$	$30.25^{+4.43}_{-4.43}$
LS220	1.16	714	SR HR	✓	95.811.3	68.9 >11.3	95.5	$0.306^{+0.153}_{-0.153}$	$0.34^{+0.00}_{-0.00}$	$0.22^{+0.00}_{-0.00}$	$0.16^{+0.00}_{-0.00}$	$34.08^{+1.00}_{-1.00}$
LS220	1.16	714	LR SR HR	X	29.5 36.1 28.8	>29.5 >36.1 24.1	$0.33^{+0.05}_{-0.05}$	$0.17^{+0.01}_{-0.01}$	$0.17^{+0.01}_{-0.01}$	$30.01^{+0.64}_{-0.64}$
LS220	1.43	710	LR SR	✓	19.8 28.5	15.7 12.3	19.6	$0.178^{+0.072}_{-0.072}$	$0.73^{+0.03}_{-0.03}$	$0.16^{+0.02}_{-0.02}$	$0.17^{+0.01}_{-0.01}$	$26.77^{+3.50}_{-3.50}$
LS220	1.66	707	LR SR	✓	6.8 8.0	1.4 2.1	2.0	$0.068^{+0.008}_{-0.008}$	$1.11^{+0.38}_{-0.38}$	$0.07^{+0.01}_{-0.01}$	$0.14^{+0.01}_{-0.01}$	$13.18^{+1.33}_{-1.33}$
SFHo	1.00	413	SR HR	✓	25.3 11.6	6.0 4.0	50.0	$0.023^{+0.012}_{-0.012}$	$0.40^{+0.07}_{-0.07}$	$0.21^{+0.00}_{-0.00}$	$0.19^{+0.01}_{-0.01}$	$32.48^{+1.79}_{-1.79}$
SFHo	1.00	413	LR SR HR	X	3.2 7.7 9.0	>3.2 4.1 3.8	7.2	$0.019^{+0.007}_{-0.007}$	$0.28^{+0.07}_{-0.07}$	$0.23^{+0.01}_{-0.01}$	$0.21^{+0.01}_{-0.01}$	$31.66^{+1.80}_{-1.80}$
SFHo	1.13	412	SR HR	✓	14.2 14.3	6.3 >14.3	$0.44^{+0.12}_{-0.12}$	$0.18^{+0.01}_{-0.01}$	$0.23^{+0.01}_{-0.01}$	$33.20^{+0.78}_{-0.78}$
SFHo	1.13	412	LR SR HR	X	16.5 19.3 15.2	5.5 11.6 3.9	15.1	$0.046^{+0.041}_{-0.041}$	$0.42^{+0.03}_{-0.03}$	$0.17^{+0.03}_{-0.03}$	$0.22^{+0.01}_{-0.01}$	$29.63^{+4.39}_{-4.39}$
SFHo	1.43	414	LR	✓	19.6	4.8	18.9	$0.201^{+0.101}_{-0.101}$	$0.38^{+0.08}_{-0.08}$	$0.14^{+0.03}_{-0.03}$	$0.20^{+0.04}_{-0.04}$	$29.20^{+5.84}_{-5.84}$
SFHo	1.43	414	SR	✓	46.5	>46.5	50.8	$0.241^{+0.121}_{-0.121}$	$0.24^{+0.05}_{-0.05}$	$0.19^{+0.04}_{-0.04}$	$0.14^{+0.03}_{-0.03}$	$32.86^{+6.57}_{-6.57}$
SFHo	1.66	408	LR SR	✓	11.2 16.8	1.3 1.3	11.6	$0.177^{+0.153}_{-0.153}$	$0.15^{+0.00}_{-0.00}$	$0.07^{+0.00}_{-0.00}$	$0.12^{+0.01}_{-0.01}$	$10.39^{+1.14}_{-1.14}$
SLy4	1.00	402	LR SR	✓	10.5 13.1	2.8 2.8	$0.09^{+0.02}_{-0.02}$	$0.23^{+0.02}_{-0.02}$	$0.27^{+0.02}_{-0.02}$	$30.81^{+2.81}_{-2.81}$
SLy4	1.00	402	LR SR	X	12.7 22.0	2.7 13.8	12.5	$0.071^{+0.175}_{-0.175}$	$0.31^{+0.20}_{-0.20}$	$0.23^{+0.03}_{-0.03}$	$0.22^{+0.01}_{-0.01}$	$32.23^{+4.84}_{-4.84}$
SLy4	1.13	402	LR SR	X	8.4 20.3	>8.4 13.0	8.0	$0.164^{+0.023}_{-0.023}$	$0.59^{+0.07}_{-0.07}$	$0.16^{+0.00}_{-0.00}$	$0.24^{+0.01}_{-0.01}$	$29.67^{+1.97}_{-1.97}$
SLy4	1.43	399	SR	✓	40.3	>40.3	45.2	$0.200^{+0.100}_{-0.100}$	$0.20^{+0.04}_{-0.04}$	$0.21^{+0.04}_{-0.04}$	$0.15^{+0.03}_{-0.03}$	$34.03^{+6.81}_{-6.81}$
SLy4	1.66	397	SR	✓	7.2	1.2	3.9	$0.138^{+0.069}_{-0.069}$	$0.28^{+0.06}_{-0.06}$	$0.05^{+0.01}_{-0.01}$	$0.12^{+0.02}_{-0.02}$	$8.43^{+1.69}_{-1.69}$

Note. The columns contain the following information, starting from the left. Equation of state, mass ratio, available resolutions, inclusion of subgrid turbulence, time of the simulation end, time of the BH formation for LR, SR, HR resolutions separately, time of last output, time the disk mass is extracted, disk mass, mass of the dynamical ejecta, mass-averaged electron fraction, terminal velocity and rms angle (from the binary plane) for dynamical ejecta. For all data except t_{BH} , t_{end} and t_{disk} , the value that is given is a mean value across resolutions, with an error estimated as one standard deviation from the mean. In a case where only one resolution is present, the error is assumed to be 20% of the value. For discussions on errors and convergence see Radice et al. (2018b) and Bernuzzi et al. (2020).

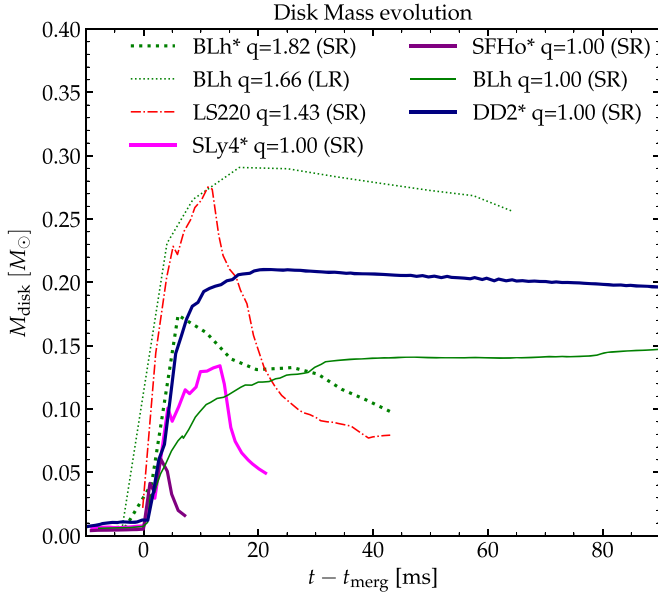


Figure 2. Time evolution of the total disk mass for a few selected short-lived and long-lived cases. The former show a rapid accretion right after disk formation. The plots show distinct differences in dynamical evolution after disk formation: accretion onto the newly formed BH (short-lived remnants) or accretion onto the NS remnant (DD2 $q = 1$) with possible continuous mass-shedding from the remnant into the disk (BLh* $q = 1$).

colder and reprocessed material near the edge with $Y_e \sim 0.4$. The maximum disk masses (at formation) are generically larger for stiffer EOS and higher mass ratio. The disk mass can be described within the numerical uncertainties by a quadratic function of the mass ratio and the reduced tidal parameters (see Section 7). In particular, the most massive disks are formed in the case of a highly asymmetric BLh $q = 1.82$ binary and of the LS220 but less asymmetric $q = 1.43$ binary with softer EOS. In the latter case the quick collapse of the remnant removes more than half of the disk mass within 40 ms postmerger.

In the long-lived cases, the disk (now defined by the material with $\rho \lesssim 10^{13} \text{ g cm}^{-3}$) is more massive and extended than the disk around BH remnants (Perego et al. 2019). In general, the maximum disk mass is larger for stiffer EOS and higher mass ratio. For example, the DD2 $q = 1$ remnant has disk mass $\sim 0.2 M_\odot$ while the BLh $q = 1$ has $\lesssim 0.15 M_\odot$. The disk of the BLh $q \sim 1.4$ – 1.5 remnant is up to a factor two more massive than the latter. The long-term disk evolution is determined by its interaction with the central object. On the one hand the gravitational pull and the neutrino cooling cause the material to accrete. On the other hand the spiral density waves continuously feed the disk with centrifugally supported material, and the angular momentum transport caused by the turbulence favors its expansion. Thus, the disk loses its mass by accretion if the central object is a BH, but can either acquire or lose mass if the central object is an NS. The latter cases are visible in Figure 2 for the BLh EOS and the DD2 EOS. In particular, the BLh* $q = 1$ postmerger configuration is such that the mass-shedding by the remnant exceeds the mass accretion. This behavior is believed to be set by a combination of the EOS softness and the treatment of the thermal effects within the BLh EOS. The former implies stronger postmerger remnant oscillations than the DD2 EOS, the latter higher remnant average temperature.

In terms of disk structure, the inclusion of turbulence appears to smoothen the mass distribution of disk properties, such as Y_e , s , T ,

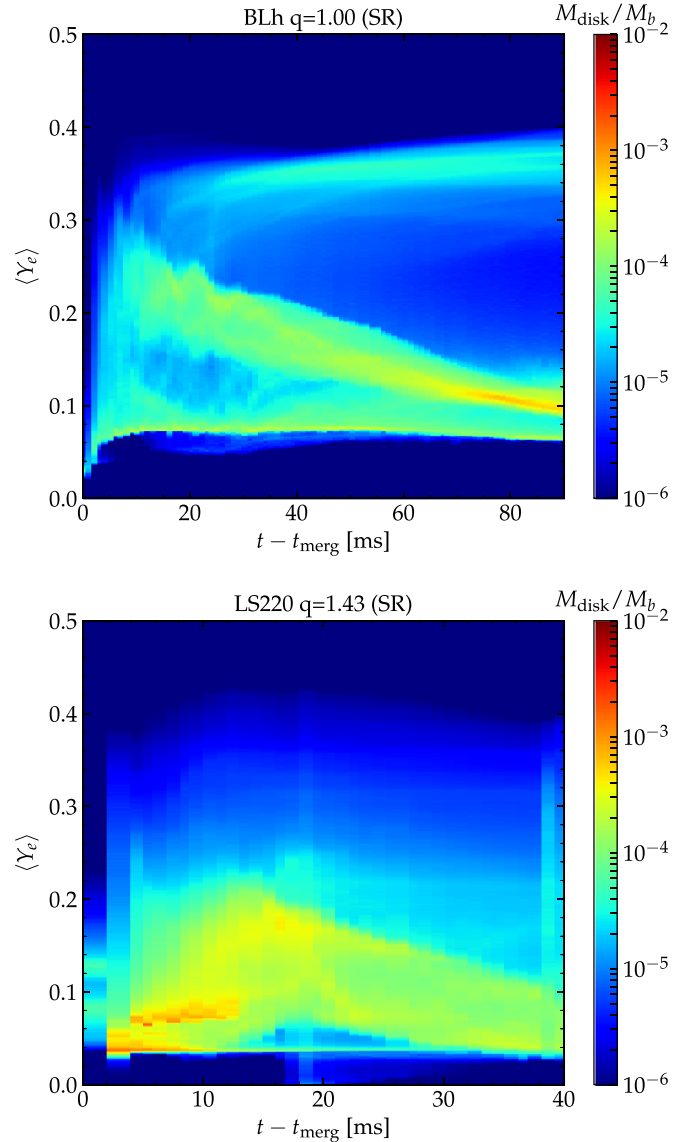


Figure 3. Evolution of the disk mass-averaged electron fraction with time for a long-lived remnant (top) and a short-lived one (bottom). The plot shows that with time the bulk of the disk lowers its Y_e via cooling, while a small fraction in terms of mass gains a high Y_e , which relates to the highly irradiated surface of the disk.

making them slightly broader. However, detailed quantitative study requires more simulations at several resolutions to separate the effects of finite-grid and subgrid turbulence (Bernuzzi et al. 2020; Radice 2020).

Disks around long-lived remnants are also more optically thick than disks around BHs. The top panel of Figure 3 shows the evolution of the mass-weighted electron fraction for the case of BLh $q = 1$ up to 90 ms. At early times a fraction of fluid elements have $Y_e \sim 0.25$ as a result of the shock and spiral waves during formation. After about ~ 40 ms from merger, most of the matter comprises a neutron-rich bulk at $Y_e \lesssim 0.1$. Neutrinos irradiate the disk edge (Figure 11, density contours), which at ~ 40 ms reaches $Y_e \sim 0.4$. Note that neutrinos in merger remnants decouple at $\rho \sim 10^{11} \text{ g cm}^{-3}$ (Endrizzi et al. 2020). While we expect this picture to be qualitatively correct, the gap at intermediate $\langle Y_e \rangle \simeq 0.15$ might be an artifact of the M0, which assumes radial propagation of neutrinos and cannot correctly capture the reabsorption of

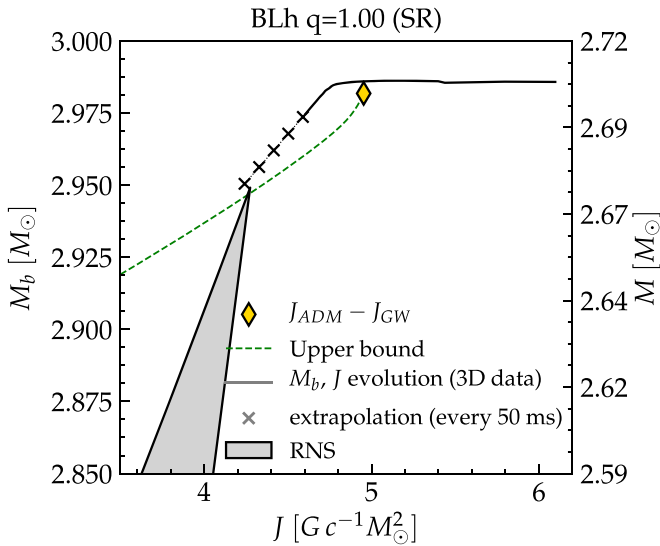


Figure 4. Diagram of baryon mass vs. angular momentum for the BLh $q = 1$ remnant. The colored diamond marks the baryonic mass and angular momentum at the end of the dynamical GW-dominated phase. After the GW phase, the evolution is driven by the massive outflows. The solid black line is the M_b and J estimated from the 3D data integrals under the assumption of axisymmetry. The green dashed line is a conservative estimate of the mass ejection and a possible trajectory for the viscous evolution as estimated in Radice et al. (2018a). The crosses are a linear extrapolation in time of the solid black line. The gray shaded region is the region of stability of rigidly rotating NS equilibria.

neutrinos emitted from the midplane of the disk. In the case of a BH remnant (bottom panel of Figure 3), the more compact disk still emits neutrinos efficiently, but neutrino absorption at the disk edge is not relevant due to the lack of emission from the massive NS, and the average electron fraction is systematically lower.

If the disk expands outward sufficiently far, recombination of nucleons into alpha particles provides enough energy to unbind the outermost material and generate mass outflows (Beloborodov 2008; Lee et al. 2009; Fernández & Metzger 2013). On the simulated timescales, mass is ejected from the remnant due to the spiral-wave wind (Nedora et al. 2019) and the neutrino-driven wind (ν -component; Dessart et al. 2009; Perego et al. 2014; Just et al. 2015). The former is powered by a hydrodynamical mechanism that preferentially ejects material at low latitudes. The spiral-wave wind can have a mass up to a few $10^{-2} M_\odot$ and velocities $\sim 0.2 c$. The ejecta have electron fraction typically larger than ~ 0.25 since they are partially reprocessed by hydrodynamic shocks in the expanding arms. The ν -component is driven by neutrino heating above the remnant. It generates outflows with smaller masses $\sim 10^{-4} M_\odot$ and larger Y_e than the spiral-wave wind. Differently from spiral-wave wind the mass flux of the ν -component in our simulations subsides before they end, due to rapid baryon loading of the polar region. The spiral-wave wind will be discussed in detail in Section 5.

The fate of the long-lived remnant beyond the simulated timescale is difficult to predict without longer, ab initio simulations in (3+1)D with complete physics. To illustrate this aspect we discuss the representative case of BLh $q = 1$ that is one of our longest runs of binaries with baryon mass larger than the one supported by the zero-temperature β -equilibrated rigidly rotating equilibrium single NS configurations. Figure 4 shows the evolution of the remnant in the diagram of baryon mass

versus angular momentum. The total baryon mass of the system is conserved, and in the absence of ejecta (e.g., during the inspiral) the binary evolves along curves of constant baryonic mass but loses angular momentum due to emission of GWs. The latter is computed from the multipolar GW following Damour et al. (2012) and Bernuzzi et al. (2012, 2015), in particular taking the difference between the Arnowitt–Deser–Misner initial angular momentum of the initial data and the angular momentum carried away by the gravitational waves by the end of the simulations. After the GW losses becomes inefficient, the remnant remains to the right with respect to the rigidly rotating equilibria region, marked as the gray shaded area in Figure 4. This indicates that the remnant has more angular momentum than the relative (same baryon mass) NS equilibrium, and this is a generic features of all the simulated binaries (Radice et al. 2018a; Zappa et al. 2018). Additionally, the baryon mass of the remnant after the GW-driven phase is larger than the maximum baryon mass for rigidly rotating equilibria. This is usually called a hypermassive NS remnant, according to a classification based on zero-temperature EOS equilibria (Baumgarte et al. 2000), and it is thus expected to collapse to a BH in a finite time. After the dynamical GW-dominated phase (yellow diamond) we compute the evolution of angular momentum and mass under the assumption of axisymmetry (black solid curve).¹¹ Massive ejecta beyond the simulated time can drive the remnant evolution to the stability limit, in contrast with the naive expectation of BH collapse. Indeed, both the extrapolation of the data at longer timescales (black crosses) and a conservative estimate of an upper bound (Radice et al. 2018a) (green dashed line) are compatible with a possible massive NS remnant close to the Keplerian limit. A linear extrapolation of the final trend indicates that if about $\approx 0.05 M_\odot$ ($\approx 40\%$ of the disk mass at the final evolution time) of the disk evaporates at the same rate, then the remnant would be close to the mass-shedding limit of rigidly rotating equilibria at about ~ 300 ms postmerger. Note this simulation is with viscosity, but magnetic stresses could further boost ejecta (Metzger et al. 2007; Bucciantini et al. 2012; Siegel & Metzger 2017; Fernández et al. 2019; Cioffi 2020).

A similar outcome is obtained for other binaries. In the case of DD2, however, remnants lie below the cusp of the equilibria region, having an excess of angular momentum but not of baryonic mass. The evolution toward stability is slower in these cases. More asymmetric models are formed with larger excess in the total angular momentum and must shed a larger amount of mass to reach the equilibrium. We estimate that the amount of ejected mass required to reach stability lies between $\sim 0.05 M_\odot$ and $0.2 M_\odot$ for the $q = 1$ and $q = 1.4$ binaries, respectively, again corresponding to $\lesssim 40\%$ of the disk mass.

4. Dynamical Ejecta

The mechanisms behind dynamical ejecta and results for our simulations have been extensively discussed in recent papers (Radice et al. 2018b; Bernuzzi et al. 2020). Here, we focus on the overall properties of the mass ejecta of our set of targeted simulations and provide approximate fitting formulae for the average mass, velocity, and electron fraction. We recall that the dynamical ejecta are here defined as the ejecta computed with the geodesic criterion discussed in Section 2.4. Then, we

¹¹ Note that the angular momentum estimated from the GW and that from the integral of Equation (8) assuming axisymmetry are compatible within the errors made in the latter estimate.

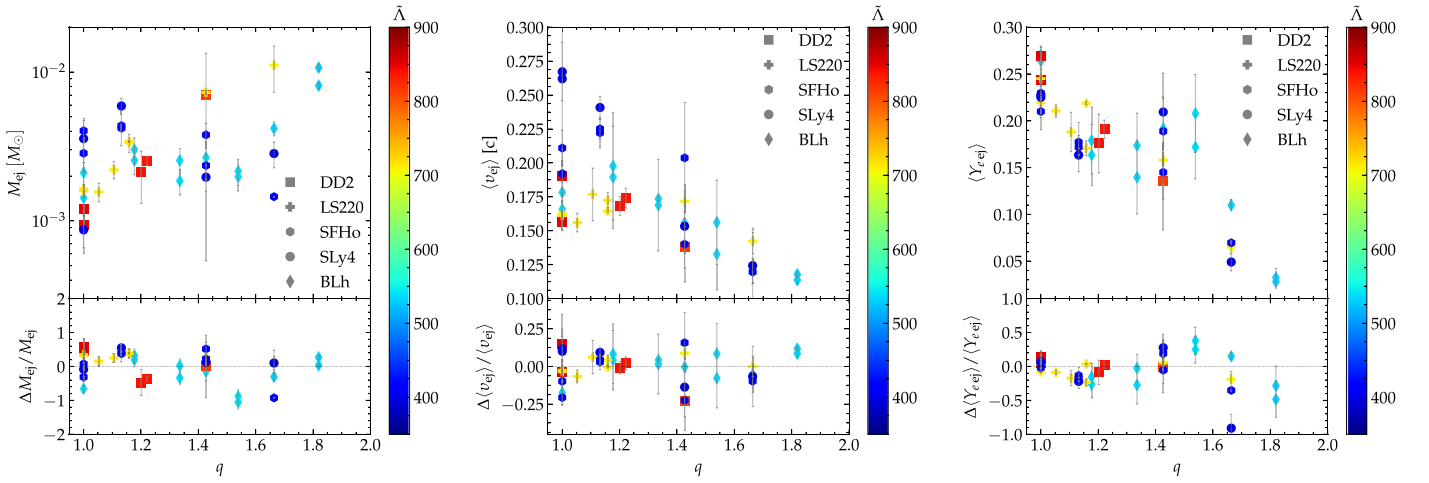


Figure 5. Dynamical ejecta properties as a function of mass ratio and reduced tidal parameter. The dependence on the latter is color-coded. From left to right the main panels show the total mass, the mass-averaged velocity, and the electron fraction. The bottom panels show the relative difference between the data and the polynomial fit discussed in the text.

Table 3
Coefficients for the Polynomial Regression with Equation (10) of the Data with Chirp Mass $\mathcal{M}_c = 1.188M_\odot$ in This Paper

	$\log_{10}(M_{\text{ej}}^{\text{d}})$	$\langle v_{\infty}^{\text{d}} \rangle (c)$	$\langle Y_e^{\text{d}} \rangle$	$M_{\text{disk}} (M_\odot)$
b_0	1.04	0.720	-3.13×10^{-2}	-1.57
b_1	-3.31	-0.204	0.284	2.07
b_2	-6.89×10^{-3}	-1.20×10^{-3}	5.89×10^{-4}	9.83×10^{-4}
b_3	0.4194	-4.05×10^{-2}	-0.148	-0.667
b_4	5.09×10^{-3}	3.92×10^{-4}	-2.02×10^{-4}	-2.55×10^{-4}
b_5	5.83×10^{-7}	5.20×10^{-7}	-2.78×10^{-7}	-4.61×10^{-7}
R^2	0.748	0.769	0.824	0.415

Note. The last row reports the coefficient of determination of the fit, R^2 .

discuss the applicability of these results for the kN AT2017gfo, associated with the gravitational-wave event GW170817.

The data presented in this work are obtained with the M0 and GRLES schemes and span a significant range in mass ratio but a smaller range in the reduced tidal parameter $\tilde{\Lambda}$ than our previous data set of Radice et al. (2018b), where most of the simulations were performed with the leakage scheme only. Comparing the data obtained with leakage and those with the M0, we observe that neutrino absorption leads not only to an increased average electron fraction but also to larger total ejected mass and velocity. For example, the mass averaged over the simulations from Table 2 is $M_{\text{ej}}^{\text{d}} = (3.442 \pm 2.495) \times 10^{-3} M_\odot$ (where hereafter we report also the standard deviation), while the same quantity calculated for data of Radice et al. (2018b) is $M_{\text{ej}}^{\text{d}} = (1.352 \pm 1.250) \times 10^{-3} M_\odot$. The mass-averaged terminal velocity of the dynamical ejecta ranges between $0.1c$ and $0.3c$, in good agreement with Radice et al. (2018b). The mass-averaged velocity, averaged over all the simulations, is $\langle v_{\infty}^{\text{d}} \rangle = (0.172 \pm 0.038)c$. The new data at fixed chirp mass show a correlation of $\langle v_{\infty}^{\text{d}} \rangle$ with the tidal parameter $\tilde{\Lambda}$: the lower $\tilde{\Lambda}$ the higher the velocity. This is a consequence of the fact that dynamical ejecta in mergers of comparable mass is dominated by the shocked component and that the shock velocity is larger the more compact the binary is¹². In contrast, for high mass ratios $q \gtrsim 1.5$, the

ejecta is dominated by the tidal component and it is characterized by smaller $\langle v_{\infty}^{\text{d}} \rangle$. The mass-averaged electron fraction in our simulations varies between 0.1 and 0.3, and averaged among the simulations it is $\langle Y_e^{\text{d}} \rangle = 0.175 \pm 0.063$. The range is broader than that previously reported in Radice et al. (2018b), where the upper limit was ≈ 0.2 and the lower was 0.1. The main difference for this result is the use of the M0 scheme, as noted above. The average electron fraction of our models with M0 neutrino transport is very similar to the ones obtained with the M1 scheme of Sekiguchi et al. (2016) and Vincent et al. (2020). Moreover, the high- q simulations where the dynamical ejecta is dominated by the tidal component contribute to the lower boundary of $\langle Y_e^{\text{d}} \rangle$. The comparison between simulations with and without the GRLES scheme does not indicate a strong effect on the dynamical ejecta; the effect is comparable to the effect of finite-grid resolution (Bernuzzi et al. 2020; Radice 2020).

Overall, we find that the properties of the ejecta depend strongly on mass ratio and the EOS softness, which can be parameterized by the reduced tidal parameter. Figure 5 shows the dynamical ejecta properties as a function of the mass ratio and (color-coded) $\tilde{\Lambda}$. We can fit our data at fixed chirp mass using a second-order polynomial in these two parameters,

$$P_2(q, \tilde{\Lambda}) = b_0 + b_1 q + b_2 \tilde{\Lambda} + b_3 q^2 + b_4 q \tilde{\Lambda} + b_5 \tilde{\Lambda}^2. \quad (10)$$

Fitting coefficients are reported in Table 3 for all the quantities; fit residuals are displayed in the bottom panel of Figure 5.

¹² Note that in the definition of prompt collapse we adopted, there is no shocked ejecta.

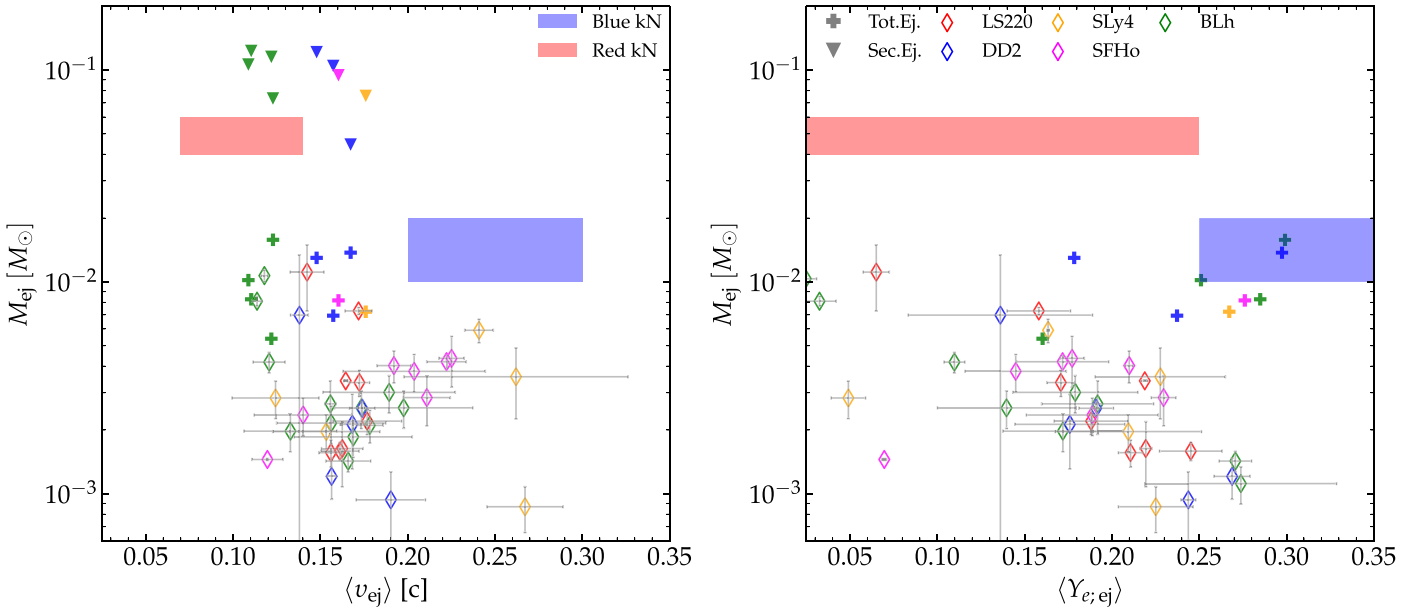


Figure 6. Summary of the ejecta properties of our models. Diamonds mark the dynamical ejecta, crosses include the contribution of the spiral-wave wind for the long-lived models, and triangles are an estimate of the total ejecta mass on a secular timescale, assuming 40% of the disk mass is unbound on secular timescales. The ejecta mass is shown in terms of the mass-averaged velocity (left) and of the averaged electron fraction (right). The filled blue and red patches are the expected values of ejecta mass and velocity for blue and red components of AT2017gfo compiled by Siegel (2019), based on Villar et al. (2017).

These fits refer to binaries with the chirp mass of GW170817, and are valid in the ranges of mass and mass ratio covered by the simulations. However, we have explored several fitting functions, including several proposals in the literature, and find that Equation (10) provides a simple and robust fitting model for all the data currently available; these results will be reported elsewhere.

Let us discuss an application of our results to GW170817. We apply the best fits using the 90% credible intervals of q and $\tilde{\Lambda}$ estimated from the LIGO–Virgo GW analysis (Abbott 2017c, 2018, 2019b; De et al. 2018), i.e. $\tilde{\Lambda} = 300^{+500}_{-190}$ and $q \in [1, 1.37]$. Using the formulae for error bars developed in Radice et al. (2018b), we find that $M_{\text{ej}}^{\text{d}} \in [0.72, 7.52] \times 10^{-3} M_{\odot}$, $\langle v_{\text{ej}}^{\text{d}} \rangle \in [0.16, 0.39]c$, and $\langle Y_{e;\text{ej}}^{\text{d}} \rangle \in [0.11, 0.23]$.

These values are not compatible with the ejecta properties inferred from AT2017gfo using spherical two-components kN models (Villar et al. 2017). Siegel (2019) estimates that the various fitting models predict $M_{\text{ej}}^{\text{red}} \in (4, 6) \times 10^{-2} M_{\odot}$ and $v_{\text{ej}}^{\text{red}} \in (0.07, 0.14)$ for the red component, while $M_{\text{ej}}^{\text{blue}} \in (1, 2) \times 10^{-2} M_{\odot}$ and $v_{\text{ej}}^{\text{blue}} \in (0.2, 0.3)$ for the blue component. Thus, neither component can be explained with the dynamical ejecta from our simulations. In Figure 6 we show the ejecta properties from all our models (diamonds) and the parameters inferred from the observations as red and blue boxes. Despite the fact that $\langle Y_{e;\text{ej}}^{\text{d}} \rangle \sim 0.15\text{--}0.25$ for BNSs of comparable masses, none of our models has dynamical ejecta massive enough to account for the red component fit. The NR data also have significantly higher velocities than the one inferred by the two-component kN model. This indicates that additional ejecta components should be considered in order to robustly associate the kN to the ejecta mechanisms (Perego et al. 2017; Kawaguchi et al. 2018; Nedora et al. 2019). The analysis of AT2017gfo with realistic ejecta models and possibly more realistic radiation transfer simulations is beyond the scope of this work, and will be performed in future work.

We will refer to Figure 6 throughout the text when discussing the spiral-wave wind and possible winds from the remnant disks.

5. Spiral-wave Wind

In this section we discuss in detail the dynamics of spiral waves and the associated spiral-wave wind. We postprocess the simulations to compute the hydrodynamical modes of the NS remnants using the method discussed in Section 2.4. The mode analysis for few representative cases is shown in Figure 7. The remnant NS is strongly deformed, with the characteristic spiral arms developing from the cores' shock interface and expanding outward (Shibata & Uryu 2000; Shibata & Taniguchi 2006; Bernuzzi et al. 2014; Kastaun & Galeazzi 2015; Paschalidis et al. 2015; East et al. 2016b; Lehner et al. 2016b; Radice et al. 2016a). At early times the main deformation is an $m = 2$ bar-shaped mode, while at later times an $m = 1$ mode becomes the dominant deformation (Bernuzzi et al. 2014; Kastaun & Galeazzi 2015; Paschalidis et al. 2015; East et al. 2016b; Lehner et al. 2016b; Radice et al. 2016a). In the short-lived LS220 $q = 1$ binary, the $m = 1$ mode is subdominant with respect to the $m = 2$, and it reaches a maximum close to the collapse (see Bernuzzi et al. 2014). Instead, in the long-lived remnant DD2 $q = 1$ the $m = 1$ mode becomes at least comparable to the $m = 2$ mode at ~ 20 ms and persists throughout the remnant's lifetime, while the $m = 2$ mode efficiently dissipates via GW emission (Bernuzzi et al. 2016; Radice et al. 2016a). With respect to the mass ratio, we observe that the magnitude of the $m = 1$ mode increases with q . In particular, BLh $q = 1.43$ and LS220 $q = 1.22$ show the largest $C_{m=1}$. Thus remnants from asymmetric binary mergers exhibit stronger $m = 1$ modes, which in turn leads to a larger spiral-wave wind mass flux. Regarding $C_{m=2}$, we observe no clear trend in q . This is in agreement with what was reported by Lehner et al. (2016b).

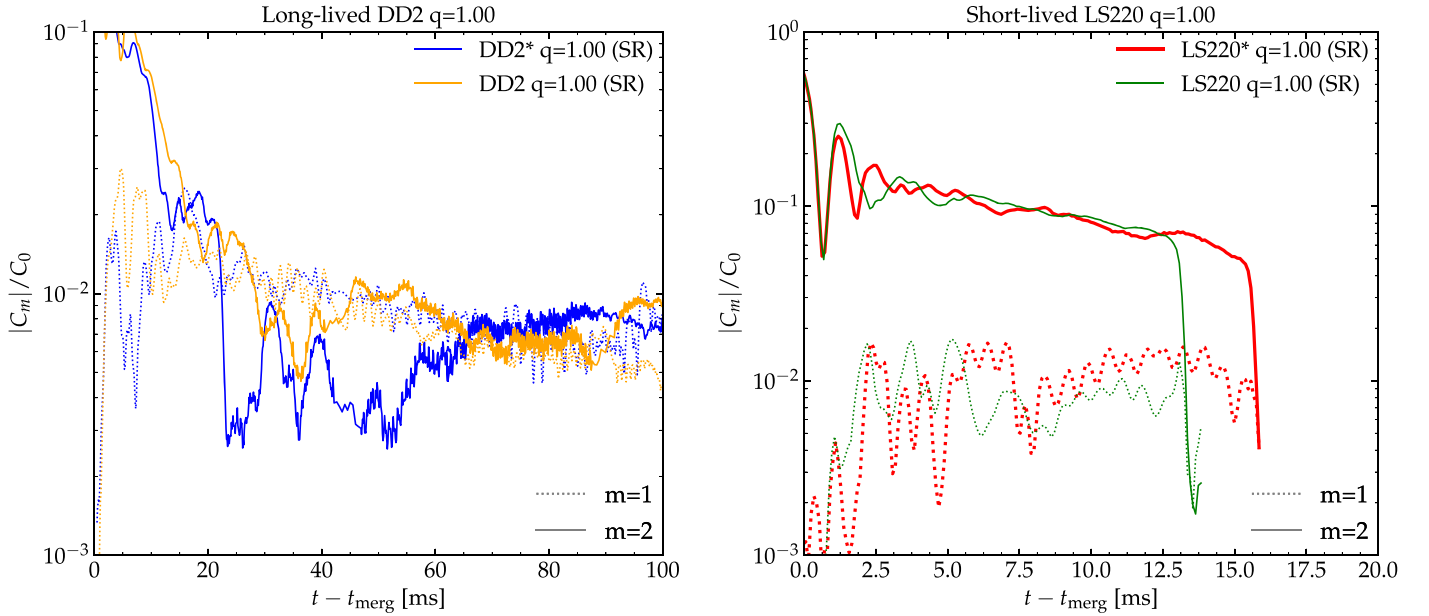


Figure 7. Mode analysis for several equal-mass long-lived and short-lived remnants. The evolution of the $m = 2$ and the $m = 1$ monitored by Equation (4) is shown for the DD2 and LS220 remnants with and without turbulent viscosity. The $m = 2$ mode in the long-lived remnant is strongly damped by the emission of gravitational radiation and becomes comparable to the $m = 1$ mode on a timescale of $\gtrsim 20$ ms. Turbulent viscosity sustains the $m = 2$ mode for a longer period. The $m = 2$ mode is instead dominant until collapse in the short-lived remnant.

The spiral arms in a remnant are a hydrodynamic effect that is present also in simulations with polytropic EOS and without weak interactions (Bernuzzi et al. 2014; Radice et al. 2016a). However, the quantitative development of these modes in a remnant is affected by the physics input. For example, Figure 7 highlights that turbulent viscosity in the DD2 remnant helps sustain the $m = 2$ mode in time, thus boosting angular momentum transport into the disk. By contrast, the $m = 1$ modes are not significantly affected by viscosity. On the other hand, viscosity effects are not significant on short timescales after merger, and do not affect the dynamics of the LS220 remnant that collapses to a BH at ~ 15 ms.

We compute the angular momentum of the NS remnant and the disk under the assumption of axisymmetry and by integrating Equation (8) using $\rho = 10^{13} \text{ g cm}^{-3}$ as a cutting density. We observe that, for all long-lived remnants, $\sim 50\%$ of the angular momentum available at formation is transported into the disk during the first ~ 20 ms. Henceforth, the disk contains about half of the total angular momentum budget, and the remnant settles on a quasi-stationary evolutionary track (see Section 3). Similarly, we estimate that spiral density modes inject $\sim 0.1\text{--}0.4 M_\odot$ of baryon mass into the disk during the first ~ 20 ms. For the same mass and mass ratio $q = 1$, the DD2 remnant sheds a larger mass into the disk than the BLh remnant, suggesting that the process might be more efficient for stiffer EOS. Binaries of unequal mass form a larger disk than those of equal mass; compare, for instance, BLh* $q = 1.82$ and LS220* $q = 1.43$ in Figure 2.

The angular momentum transported into the disk is shown in Figure 8 for the DD2* and BLh* $q = 1$ remnants. The angular momentum is transported by waves propagating in the disk. These correspond to the spiral density waves in the remnant with $m = 1, 2$ geometry described above. The angular momentum transported during the first waves is larger for the more massive DD2 disk than for the BLh. DD2* and BLh* show some qualitative differences in their evolution starting at ~ 20 ms postmerger. While the DD2* remnant continues to

accrete and its disk decreases in mass, the BLh* remnant keeps on shedding more material into the disk than it accretes; see Figure 2 and discussion in Section 3. The reason is the strong angular momentum flux from the central region in the BLh* case as well as the higher temperature reached in this model, which lowers the rotational frequency at which mass-shedding takes place (Kaplan et al. 2014). A comparison between BLh* and BLh $q = 1$ data shows that, as expected, the angular momentum transport is enhanced in the case when turbulence is included. More simulations of the long-lived remnant evolution are required to investigate the effects of mass ratio and subgrid turbulence.

Spiral density waves in long-lived remnants trigger a massive spiral-wave wind (Nedora et al. 2019). The spiral-wave wind is computed with the Bernoulli criterion described in Section 2.4. Summary data are reported in Table 4. We recall that the spiral-wave wind is here defined as the ejecta computed with the Bernoulli criterion discussed in Section 2.4, and computed at times after which the dynamical ejecta have saturated.

Figure 9 shows the total unbound mass of the wind as a function of time. The wind is monitored after the mass flux of the dynamical ejecta (computed according to the geodesic criterion) has saturated. Mass outflows due to the spiral-wave wind continue throughout the duration of the simulations with no indication of saturation. Indeed, while injection of mass and angular momentum from the high-density core of the remnant into the disk decreases with time as the system becomes more stationary, the mass ejection is expected to continue for as long as the spiral waves persist. Because the $m = 1$ modes are not efficiently damped (Paschalidis et al. 2015; Radice et al. 2016a; Lehner et al. 2016b; East et al. 2016a), the ejection can in principle continue for the timescales that the system needs to reach equilibrium or to collapse to a BH (Section 3).

The largest wind masses are obtained for asymmetric binaries such as BLh $q = 1.67$ and LS220 $q = 1.4$, which in about ~ 50 ms unbind $\sim 0.02 M_\odot$ at a rate of $\sim 0.5 M_\odot \text{ s}^{-1}$. We

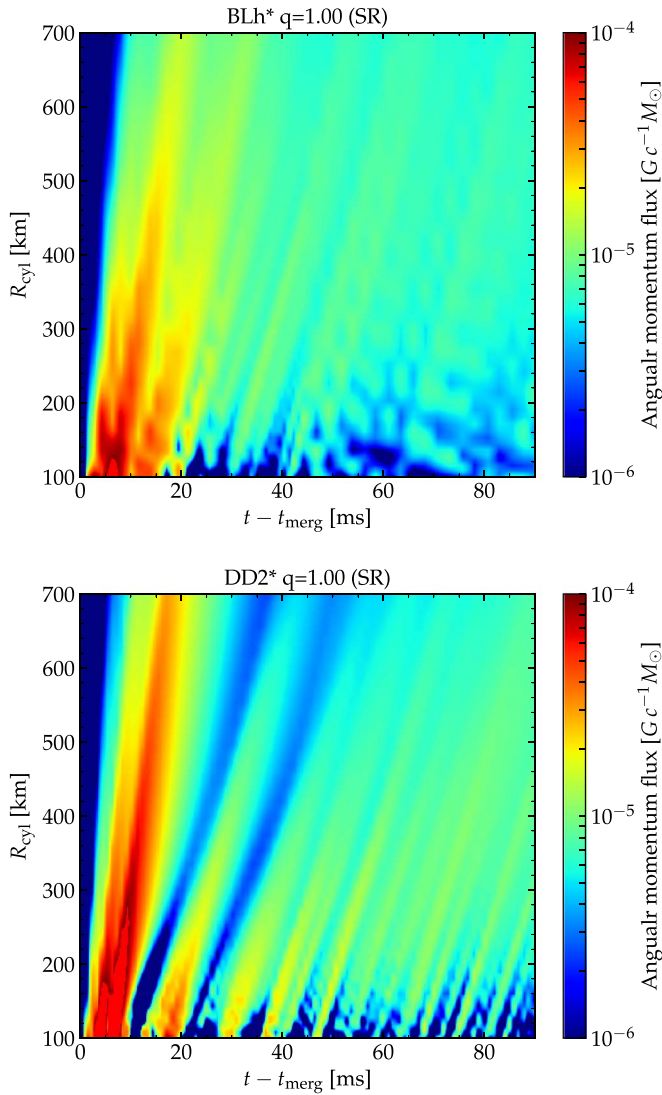


Figure 8. Angular momentum flux through consecutive cylindrical surfaces identified by cylindrical radii from $R_{\text{cyl}} = 100$ to $R_{\text{cyl}} = 500$. The plot shows the angular momentum transport into the disk.

find that models with softer EOS achieve higher mass flux at lower mass ratios, i.e., the mass flux of BLh* $q = 1.66$ is achieved by LS220* with $q = 1.22$. This might be attributed to softer EOS models having a stronger $m = 1$ mode in the remnant (see Section 7). However, if these remnants collapse, the spiral-wave mechanism shuts down and the outflow terminates. Thus the total mass ejected via spiral-wave wind depends directly on the lifetime of the remnant in addition to the binary parameters, EOS, and mass ratio.

Thermal effects play an important role in determining the outflow properties, because high thermal pressures result in more extended disks with material that is easier to unbind. The highest temperatures in our simulations are found for the BLh EOS. On longer timescales than those simulated, the spiral-wave wind from the remnants with stiffer EOS might be larger, also in relation to the larger disk masses (Section 3). Overall, the spiral-wave wind from the long-lived remnant has a mass flux $\geq 0.4 M_{\odot} \text{ s}^{-1}$.

The properties of the spiral-wave wind are found to be remarkably uniform across our simulated sample of remnants. In Figure 10, we show mass histograms of the wind angular

distribution, velocity, and electron fraction. The ejecta mass is distributed around the orbital plane in a large solid angle, similarly to the dynamical ejecta. The electron fraction is broadly distributed in $0.1 \lesssim \langle Y_e \rangle \lesssim 0.4$ and peaks around ~ 0.35 . Notably, the neutron-rich tail of the distribution is determined by the spiral-wave wind at early times, before the quasi-steady-state outflow sets in. The velocity peaks above $\sim 0.1 c$ for a softer EOS and around $\sim 0.2 c$ for a stiffer EOS. If this picture is confirmed by future simulations, this would imply an EOS-dependent distinct feature in the electromagnetic counterpart. In particular, the observation of a fast blue kN given by the spiral-wave wind should be associated with a stiff EOS.

Assuming that the source of AT2017gfo was a long-lived remnant surviving for at least $\mathcal{O}(100)$ ms, the spiral-wave wind would significantly contribute to the kN. In Figure 6 we report the total (dynamical + spiral-wave wind) ejecta mass and mass-averaged velocity for the simulated long-lived BNS (crosses). The ejecta mass and electron fraction in BLh $q = 1.18, 1.42$ and DD2 $q = 1$ are compatible with the blue component inferred using the two-component kN fit (Villar et al. 2017). However, the velocity is significantly lower than that estimated using models of Villar et al. (2017). Note that a multicomponent fitting model that explicitly accounts for the spiral-wave wind can fit the early blue emission from AT2017gfo (Nedora et al. 2019). The emission from lanthanide-rich ejecta, however, cannot be explained by the ejecta launched within the first ~ 100 ms of the remnant evolution. It is thus necessary to consider mass outflows on a longer timescale, as we shall discuss below (Lee et al. 2009; Fernández & Metzger 2016; Siegel & Metzger 2017; Fujibayashi et al. 2018; Fernández et al. 2019; Radice et al. 2018a).

6. Neutrino-driven Wind

We study in more detail the polar component of the Bernoulli ejecta and suggest that the outflow above the remnant is mostly driven by neutrino absorption rather than by the spiral-wave mechanisms. Neutrino interactions above the remnant produce a baryonic outflow that develops parallel to the rotational axis on timescales of $\sim \mathcal{O}(10)$ ms postmerger (Perego et al. 2014). Inside this wind, rotational support creates a funnel around the rotational axis as shown in Figure 11. In the figure we present the electron fraction, the Bernoulli parameter $-hu_r$, and the heating energy rate due to electron antineutrino absorption $Q_{\text{abs}; \bar{\nu}_e}$ divided by $D = W\rho\sqrt{\gamma}$ (the fluid’s conserved rest-mass density) for the BLh $q = 1$ remnant. We consider both the (x, z) and (x, y) planes, while in the right panels we focus on the innermost part of the remnant. The electron fraction in the polar region with angle from binary plane $\theta > 60^\circ$ reaches $Y_e \sim 0.35$ due to the absorption of electron-type neutrinos. Neutrino heating is maximal close to the bottom of the funnel where the ν -component originates. This corresponds to densities $\rho \sim 10^{11} \text{ g cm}^{-3}$ in the vicinity of the neutrino decoupling region (Endrizzi et al. 2020). Large magnetic fields can further boost and stabilize the collimated outflow in the polar region (Bucciantini et al. 2012; Ciolfi 2020; Mösta et al. 2020).

We confirm that the high-latitude outflows constitute a ν -component by studying the correlation between the Bernoulli parameter $-hu_r$ and E_ν/D . Moreover, we verified that simulations without neutrino heating (i.e., employing only a leakage scheme) do not have this mass ejecta in the polar

Table 4
Summary Table of the Spiral-wave Wind Properties of Long-lived Remnants

EOS	q	Resolution	GRLES	t_{end} (ms)	M_{ej}^w ($10^{-2} M_{\odot}$)	$M_{\text{ej}}^w / \Delta t$ ($M_{\odot} \text{ s}^{-1}$)	$\langle Y_e \rangle$	$\langle v_{\infty}^w \rangle$ (c)	$\langle \theta_{\text{ej}}^w \rangle$ (deg)
BLh	1.00	SR HR LR	✓	43.3 91.8 23.1	$0.39^{+0.07}_{-0.07}$	$0.70^{+0.32}_{-0.32}$	$0.31^{+0.01}_{-0.01}$	$0.12^{+0.01}_{-0.01}$	$27.06^{+2.61}_{-2.61}$
BLh	1.00	SR	X	103.2	$1.12^{+0.57}_{-0.57}$	$1.07^{+0.21}_{-0.21}$	$0.34^{+0.01}_{-0.01}$	$0.12^{+0.02}_{-0.02}$	$15.72^{+2.00}_{-2.00}$
BLh	1.18	LR	✓	69.4	$1.28^{+0.64}_{-0.64}$	$1.23^{+0.25}_{-0.25}$	$0.33^{+0.01}_{-0.01}$	$0.11^{+0.02}_{-0.02}$	$14.98^{+2.00}_{-2.00}$
BLh	1.43	LR SR	✓	35.1 59.6	$0.75^{+0.18}_{-0.18}$	$1.06^{+0.67}_{-0.67}$	$0.27^{+0.01}_{-0.01}$	$0.09^{+0.01}_{-0.01}$	$19.43^{+2.22}_{-2.22}$
BLh	1.54	LR	✓	45.8	$0.63^{+0.32}_{-0.32}$	$0.44^{+0.09}_{-0.09}$	$0.32^{+0.01}_{-0.01}$	$0.10^{+0.02}_{-0.02}$	$21.46^{+2.00}_{-2.00}$
BLh	1.66	LR SR	✓	64.6 20.1	$0.12^{+0.09}_{-0.09}$	$0.37^{+0.34}_{-0.34}$	$0.33^{+0.05}_{-0.05}$	$0.13^{+0.01}_{-0.01}$	$52.08^{+20.89}_{-20.89}$
DD2	1.00	LR SR HR	✓	123.0 113.0 74.4	$1.25^{+0.14}_{-0.14}$	$1.30^{+0.19}_{-0.19}$	$0.30^{+0.01}_{-0.01}$	$0.17^{+0.00}_{-0.00}$	$14.88^{+0.87}_{-0.87}$
DD2	1.20	LR SR HR	X	37.3 91.0 55.2	$0.48^{+0.09}_{-0.09}$	$0.74^{+0.24}_{-0.24}$	$0.26^{+0.01}_{-0.01}$	$0.15^{+0.00}_{-0.00}$	$24.54^{+2.23}_{-2.23}$
DD2	1.43	LR SR	✓	37.7 62.0	$0.60^{+0.02}_{-0.02}$	$0.51^{+0.06}_{-0.06}$	$0.23^{+0.12}_{-0.12}$	$0.16^{+0.00}_{-0.00}$	$21.74^{+0.03}_{-0.03}$
SFHo	1.43	SR	✓	46.5	$0.58^{+0.30}_{-0.30}$	$0.43^{+0.09}_{-0.09}$	$0.31^{+0.01}_{-0.01}$	$0.17^{+0.02}_{-0.02}$	$22.67^{+2.00}_{-2.00}$
SLy4	1.43	SR	✓	40.3	$0.53^{+0.27}_{-0.27}$	$0.38^{+0.08}_{-0.08}$	$0.29^{+0.01}_{-0.01}$	$0.18^{+0.02}_{-0.02}$	$23.52^{+2.00}_{-2.00}$

Note. The columns contain the following information, starting from the left. Equation of state, mass ratio, available resolutions, inclusion of subgrid turbulence, time of the simulation end, mass of the spiral-wave wind, mass-loss rate via spiral-wave wind, mass-averaged electron fraction, terminal velocity, and finally rms angle for spiral-wave wind. For these four quantities we give the mean value among the resolutions and 1σ deviations. For binaries for which only one resolution is present, the error is assumed to be 20% of the value.

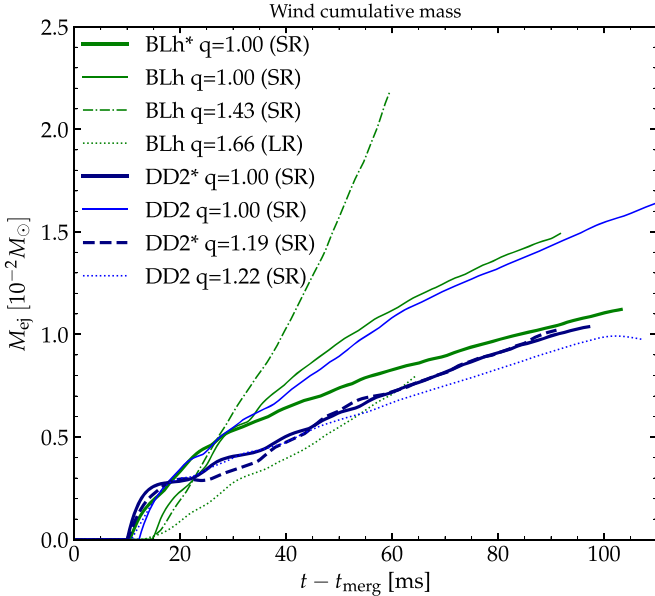


Figure 9. Cumulative mass of the spiral-wave wind from long-lived remnants. The wind persists on timescales of $\mathcal{O}(100)$ ms with mass fluxes $\sim 0.33\text{--}1.23 M_{\odot} \text{ s}^{-1}$.

region. A robust distinction between the ν -component and the spiral-wave wind is impossible to draw at intermediate latitudes ($\theta \sim 45^\circ$), where both mechanisms are at work. The mass of the ν -component can be estimated by either taking the ejected material with $\theta > 60^\circ$ or selecting $Y_e > 0.35$. Contrary to the main component of the spiral-wave wind, we find that, for both criteria, the mass flux of the ν -component is time-dependent, exhibiting strong growth after merger with a rapid decay in time. For most models, by the end of the run, the mass flux saturates, resulting in a total of $\sim 10^{-3}\text{--}10^{-4} M_{\odot}$ being ejected. We trace the cause of this flow interruption back to the presence of high-density material that is lifted by thermal pressure from the disk and pollutes the polar regions. The properties of this outflow are qualitatively similar to those discussed in, e.g., Dessart et al. (2009), Perego et al. (2014), and Fujibayashi et al. (2020b). In some of these models the

ν -component develops over longer timescales than those considered here, it achieves a quasi-steady state, and it possibly unbinds larger masses. These differences could result from the conservative choices we have made in isolating the contribution of the ν -component and in the lack of spiral-wave wind in the other models. Moreover, it could be that the right conditions for the formation of a steady ν -component might not have been reached in our simulations yet.

7. Remnant Disk Structure

We now discuss the disk structure in long-lived remnants at the end of our simulations, namely at $\sim 60\text{--}100$ ms postmerger, and the final disk masses of all our models.

We find that disks around remnant are geometrically thick, with an rms opening angle of $\langle \theta \rangle_{\text{rms}} \sim 60^\circ$, rather independent of the EOS and q . Meanwhile, the radial extent is larger for softer EOS and for larger q . The final disk masses range between $\sim 0.1 M_{\odot}$ and $\sim 0.4 M_{\odot}$ (see Table 2); smaller masses are obtained for short-lived remnants and for equal-mass binaries. The mean value and standard deviation are $\bar{M}_{\text{disk}} = (0.161 \pm 0.083) M_{\odot}$. Similarly to what we did for the dynamical ejecta, we fit the disk masses with a second-order polynomial in $(q, \bar{\Lambda})$. The coefficients of Equation (10) for this fit are given in Table 3. A more detailed study with various fitting formulae and extended data sets from the literature is reported in a companion paper (V. Nedora et al. 2020, in preparation).

The disk composition at $\sim 60\text{--}100$ ms postmerger is not uniform, as shown for BLh $q = 1$ in Figure 12, and we study it using the mass-weighted histogram reported in Figure 13. The entropy and the electron fraction show a bimodal distribution, which is more prominent for equal-mass binaries and less prominent for those with large q . The mass-weighted distribution of the entropy shows a dominant peak at low entropy $s \sim 5\text{--}10 k_B/\text{baryon}$. This peak is rather independent of EOS and q and it corresponds to the inner, mildly shocked material. The second, subdominant peak is located at larger entropies, $s \sim 15\text{--}22 k_B/\text{baryon}$, and it is more dependent on the EOS model: for softer EOSs a larger amount of mass reaches a larger entropy, while for more asymmetric binaries the second peak is centered around lower values of the entropy.

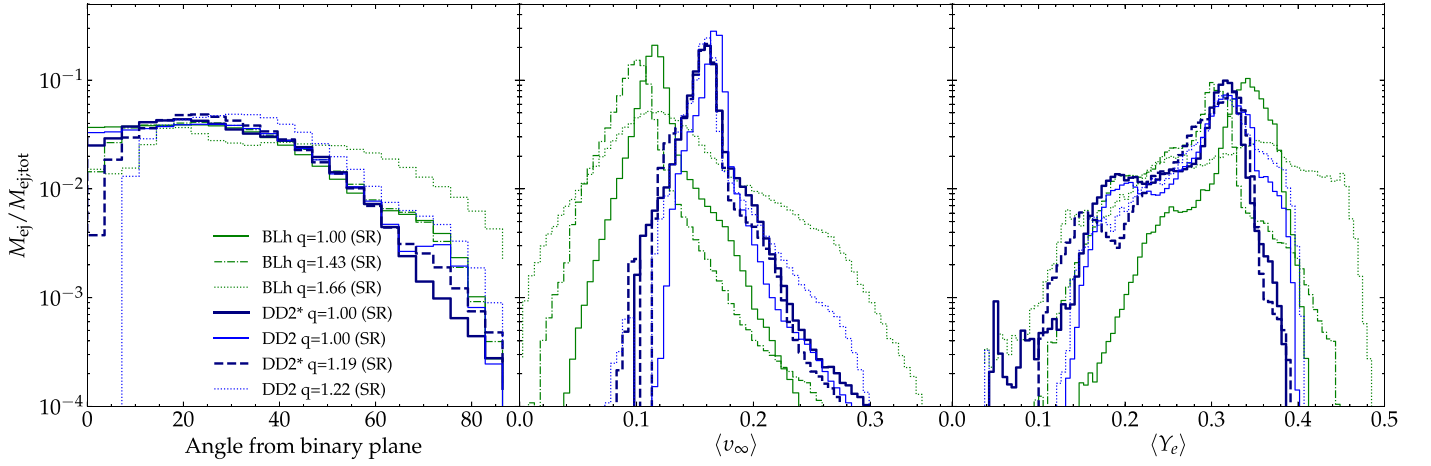


Figure 10. Mass-averaged histograms of the spiral-wave wind for a selected subset of long-lived remnant. From left to right: ejecta angular distribution, ejecta terminal velocity, and electron fraction. Remnants from more asymmetric binaries produce winds with broader angular distribution. The spiral-wave wind from the DD2 EOS remnants has higher velocity than the wind from the softer BLh EOS. The electron fraction peaks at ~ 0.3 and it is distributed from 0.1 to 0.4.

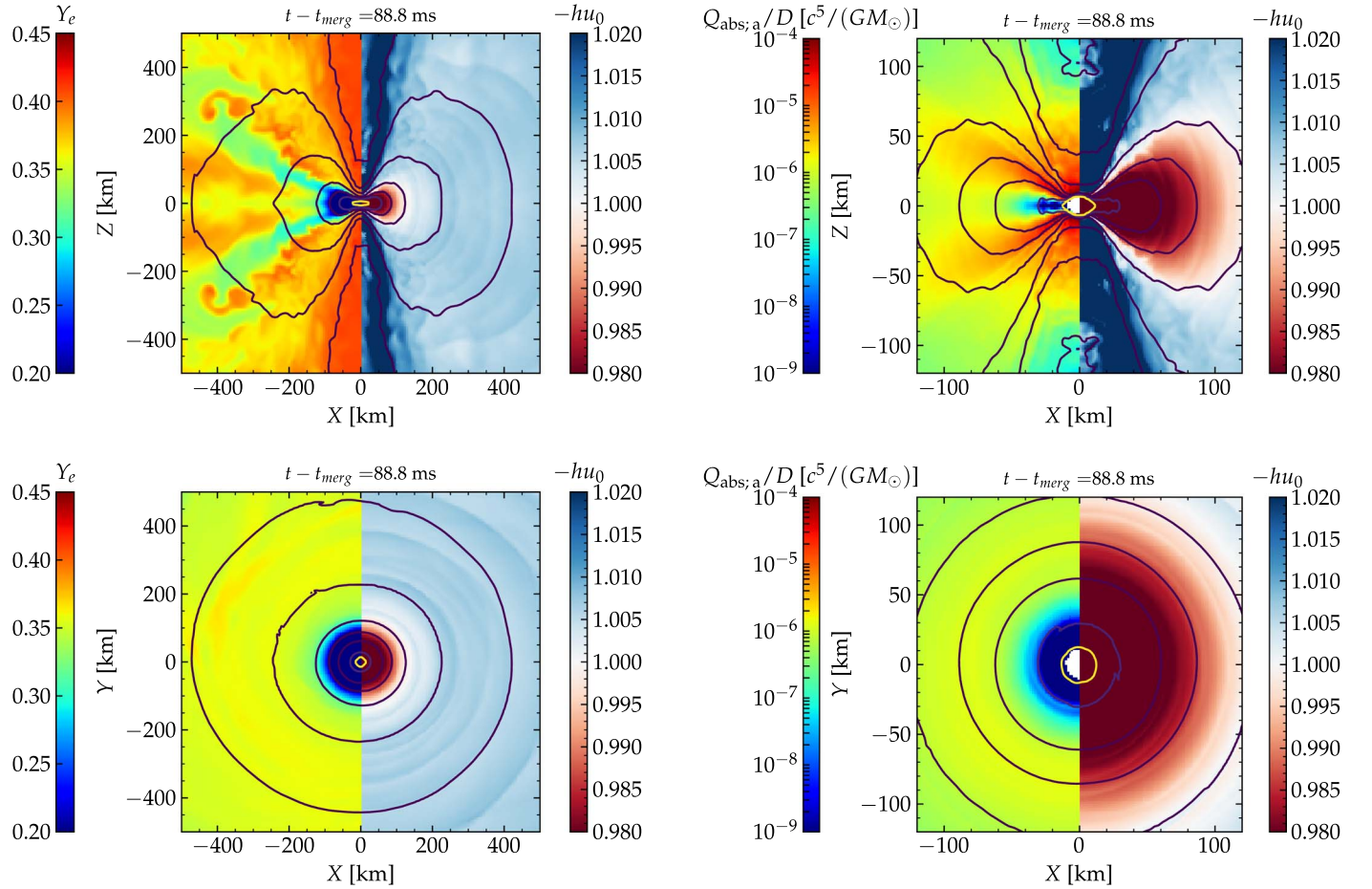


Figure 11. Snapshot of the (x, z) and (x, y) slices of the BLh $q = 1$ model at ~ 89 ms after merger. Left panels: electron fraction and $-hu_0$. High Y_e values indicate neutrino postprocessing and irradiation. $-hu_0 > 1$ indicates the material that gains enough energy to become unbound at infinity. Right: $-hu_0$ and the absorption energy rate $Q_{\text{abs},a}$ of electron antineutrinos normalized to the fluid density D .

Similarly, we observe a first peak in the Y_e distribution, around $Y_e \sim 0.1$, which corresponds to the neutrino-shielded bulk of the disk. The second (subdominant in mass) peak is at $Y_e \sim 0.3\text{--}0.4$ and it corresponds to the irradiated disk surface. We stress that, for both the entropy and the electron fraction, the two peaks refer to different regions inside the disk, as is

visible in Figure 12. Most of the matter in the disk has a temperature in the range $T \sim 1\text{--}10$ MeV. The inner part of the disk is hotter than the edge. The temperature distribution is also weakly independent of the EOS and mass ratio.

Nuclear recombination is expected to unbind a fraction of the disk mass on secular timescales of a few seconds, longer than

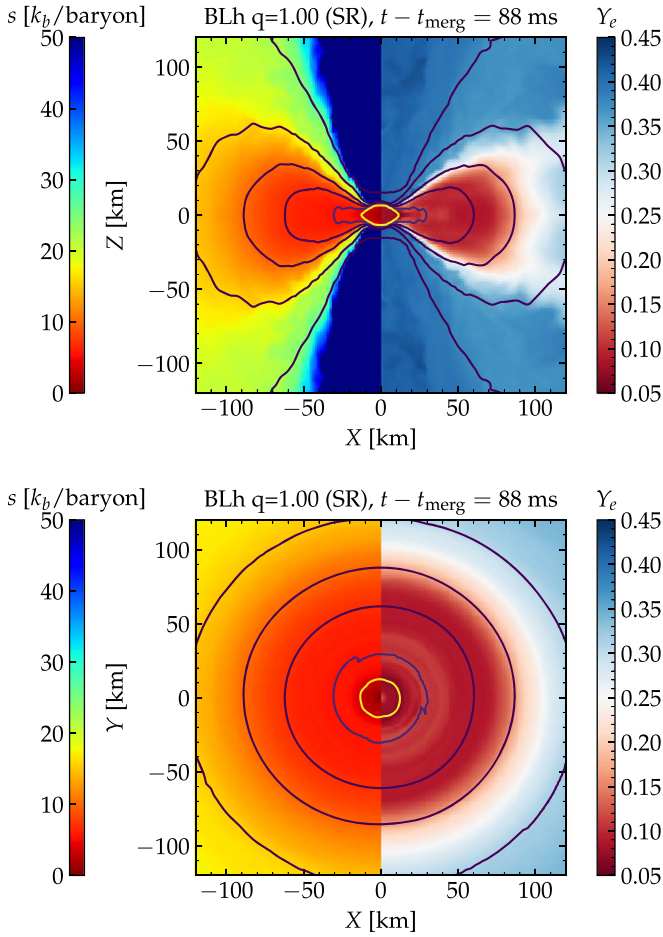


Figure 12. Entropy and electron fraction on the (x, z) plane (top) and (x, y) plane (bottom) for the remnant of BL $q = 1$ at the end of the simulation. Each plot is divided vertically, with entropy being color-coded on the left and electron fraction on the right. Solid contours indicate rest-mass density. Counting from the center, the values are $[10^{13}, 10^{12}, 10^{11}, 10^{10}, 10^9] \text{ g cm}^{-3}$, with the innermost contour encompassing the remnant.

those simulated here. Simulations and analytical estimates indicate that up to $\sim 40\%$ of the disk would become unbound due to viscous processes, with typical velocities of the order of $\lesssim 0.1 c$ (Lee et al. 2009; Fernández & Metzger 2016; Wu et al. 2016; Siegel & Metzger 2017; Fujibayashi et al. 2018, 2020b; Fernández et al. 2019; Radice et al. 2018a). Assuming these values, the mass of the secular wind from our simulated remnant disks would amount to $\sim 0.05 M_{\odot}$. We include this estimate of secular wind in Figure 6 for the long-lived remnants (lower triangles). The estimated mass is sufficient to explain the red component of AT2017gfo, as inferred from the two-components kN models of Villar et al. (2017).

8. Nucleosynthesis

The nucleosynthesis calculations are performed in post-processing following the same approach as in Radice et al. (2016b, 2018b) using the results from the nuclear reaction network Skynet of Lippuner & Roberts (2015). We report the abundances as a function of the mass number A of the different isotopes synthesized by the r -process 32 years after the merger in the material ejected from the system. Comparing to our previous study (Radice et al. 2018b), the new simulations allow us to investigate the nucleosynthesis in more detail in the presence of neutrino absorption, the contribution of the spiral-

wave wind in long-lived remnants, and the effect of mass ratio up to $q \sim 1.8$.

Figure 14 shows the nucleosynthesis yields from the dynamical ejecta (short-lived remnants) and from the dynamical ejecta + wind (long-lived remnants). We compare the abundances inferred from the simulations with up-to-date solar residual r -process abundances from Prantzos et al. (2020) (for a review of the solar system abundances, see, e.g., Pritychenko 2019). To compare the different distributions, we shift the abundances from our models such that they are always the same as the solar one for $A = 195$. Notably, all the r -process peaks are reproduced by the nucleosynthesis in the ejecta expelled by the long-lived DD2 and BLh models. This demonstrates that the complete solar r -process abundances can be recovered if the remnant is long-lived and shows the presence of a spiral-wave wind. This is a consequence of the robust properties of the latter. The possibility of short-lived binaries reproducing the solar first and second r -process peaks, at $A \sim 75$ and $A \sim 125$, respectively, strongly depends on the mass ratio. Higher- q binaries, whose dynamical ejecta is mostly of tidal tail origin with very low electron fraction, show severe underproduction of light r -process material. In contrast, $q \sim 1$ binaries reproduce both peaks reasonably well. This is the result of the inclusion of neutrino reabsorption because it increases Y_e of the shocked component of the ejecta, (Wanajo et al. 2014; Radice et al. 2018b).

We find that actinides ($A \sim 230$) are produced in all our models, but their abundances depend sensitively on the mass ratio. Very asymmetric binaries produce larger amounts of low- Y_e ejecta, which results in an increased production of actinides, broadly compatible with the solar pattern. Interestingly, only the binaries with the highest mass ratio are able to produce at the same time abundances close to solar for the third r -process peak and for actinides around ^{232}Th . This suggests that asymmetric mergers (or, alternatively, black-hole neutron-star (BHNS) mergers), might play an important role in the production of the heaviest elements through r -process nucleosynthesis.

For long-lived binaries the dynamical ejecta amounts only to a small fraction of the total mass of material leaving the system, while the spiral-wave wind is the more massive ejecta in our simulations. In the bottom right panel of Figure 14 we show how the inclusion of the spiral-wave wind changes the abundances of two representative models. Due to its overall high electron fraction, the spiral-wave wind (see Figure 10) primarily produces first-peak r -process elements, $A < 95$. Since the abundances are normalized to the third peak, the relevant differences are those in the first and second peaks. We observe that due to the slightly higher average electron fraction of the BLh outflows (Figure 10), it produces more light elements, $A \sim 75$, than the DD2 binary. Both binaries, however, display abundance pattern noticeably close to solar.

In addition to the dynamical ejecta and spiral-wave wind, the r -process nucleosynthesis occurs in the neutrino-driven wind and the secular wind from the disk. In the neutrino-driven winds, neutrino irradiation of the expanding ejecta considerably increases the electron fraction. If the velocity of the ejecta is sufficiently low, the material reaches a weak equilibrium with neutrinos in optically thin conditions, and $Y_e \leq 0.45$ (Qian & Woosley 1996). This will further boost weak r -process nucleosynthesis of light elements, $A < 130$ (Dessart et al. 2009; Perego et al. 2014; Just et al. 2015; Martin et al. 2015; Foucart et al. 2016). The viscous

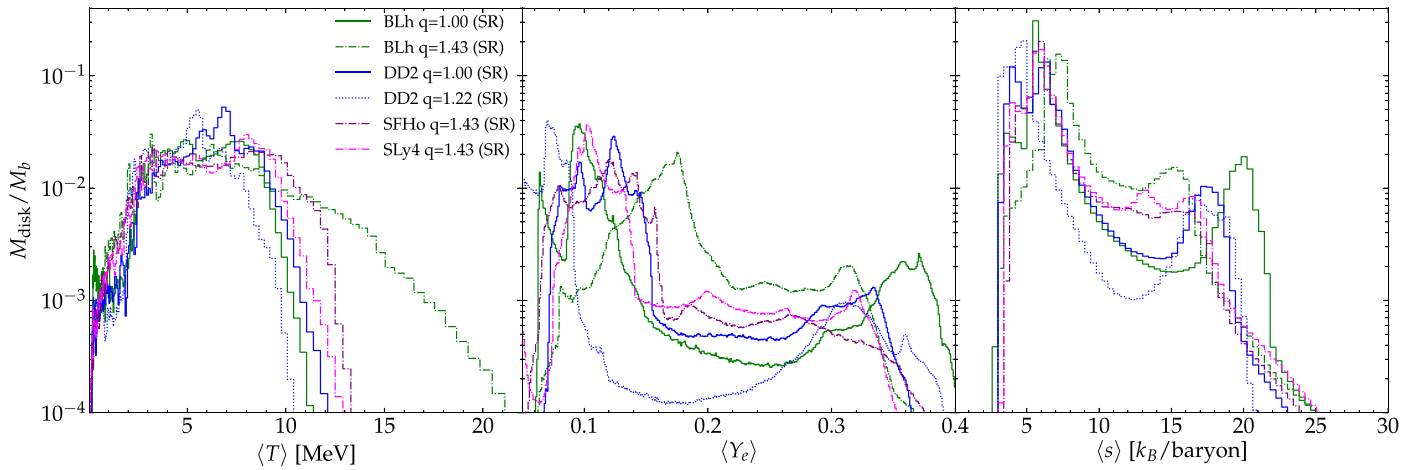


Figure 13. Composition of the disks at the end of the simulations of long-lived remnants. The histograms refer to the temperature T (left), electron fraction Y_e (middle), and entropy s (right).

and recombination-driven wind is expected to constitute the bulk of the disk outflow, but this takes place on longer timescales than those considered here. Simulations of such systems (Fernández & Metzger 2013; Just et al. 2015; Wu et al. 2016; Siegel & Metzger 2017; Fernández et al. 2019; Fujibayashi et al. 2018) suggest that this component of the outflow will have a broad range of Y_e and will synthesize both light and heavy r -process nuclei. However, heavy r -process production might be suppressed in the case of long-lived massive NS remnants (Metzger & Fernández 2014; Lippuner et al. 2017).

9. Conclusion

In this work we have discussed the long-term postmerger dynamics of 37 binaries with chirp mass $\mathcal{M}_c = 1.188 M_\odot$ compatible with the source of GW170817, gravitational mass spanning the range $M \in [2.73, 2.88] M_\odot$, and mass ratio values $q \in [1, 1.8]$. Our models were computed with five microphysical EOSs compatible with nuclear and astrophysical constraints. Each binary was simulated at multiple resolutions for a total of 76 simulations. Several simulations were pushed to ~ 100 ms postmerger. Together with our previous data (Bernuzzi et al. 2016, 2020; Radice et al. 2016b, 2017, 2018a, 2018b, 2018c; Perego et al. 2019; Endrizzi et al. 2020) these simulations form the largest sample of merger simulations with microphysics available to date. Our ejecta data are publicly available at doi:10.5281/zenodo.4159620.

The outcome of the merger was found to be very sensitive to the assumed EOS and to the mass ratio (Radice et al. 2020; Bernuzzi 2020; Bernuzzi et al. 2020). Soft EOSs and/or large mass ratios result in short-lived remnants or prompt collapse to a BH. Stiffer EOSs and mass ratio closer to one result in longer-lived, possibly stable remnants. In agreement with our previous findings, our new simulations also show that the lifetime of the remnants and the accretion disk masses are strongly correlated for binaries of comparable mass (Radice et al. 2018b, 2018c). Binaries with large mass ratio ($q \gtrsim 1.4$) have larger accretion disks than those with comparable mass, and produce massive accretion disks and tidal ejecta even when prompt BH formation occurs (see also Bernuzzi et al. 2020).

The material in the disks can reach high temperatures, O (10 MeV), especially for mergers in binaries of comparable mass, in which the disk material predominantly originates at the collisional interface between the NSs. Due to the high

temperatures, the disk material is initially reprocessed to intermediate values of the electron fraction $Y_e \simeq 0.25$. However, the disks tend to evolve to a lower Y_e of about 0.1, as expected from the theory of neutrino-dominated accretion flows (Beloborodov 2008; Siegel & Metzger 2018).

Over long timescales, the evolution of these remnants is the result of a complicated interplay between matter accretion, driven by viscous stresses and neutrino cooling, and matter ejection, driven by neutrino reabsorption and hydrodynamical torques (spiral waves; Radice et al. 2018a). Our results indicate that mass ejection due to winds can be sufficiently efficient to prevent the collapse of remnants that have initial masses above the limit supported by uniform rotation, the so-called hypermassive NSs. The determination of the ultimate fate of binaries with masses that are intermediate between prompt collapse and the maximum mass of nonrotating NSs will necessarily require long-term 3D neutrino-radiation general relativistic MHD simulations.

We studied the dynamical ejection of matter during the mergers as a function of the EOS and mass ratio. The main differences with respect to our previous systematic study (Radice et al. 2018b) are that (1) the new simulations are targeted to GW170817, so they span a smaller range of total masses; (2) the new simulations were all performed with the M0 scheme for approximate neutrino transport and the GRLES subgrid model for MHD turbulence; (3) our new simulations cover a much broader range of mass ratios. We find that the inclusion of neutrino reabsorption systematically increases the ejecta mass, as anticipated in Sekiguchi et al. (2015) and Radice et al. (2018b). The ejecta composition in our simulations is compatible with that of Sekiguchi et al. (2016) and Vincent et al. (2020), who use very different approximation schemes for neutrinos. This suggests that modern NR simulations are able to capture at least the leading-order neutrino effects reliably. We find that as the mass ratio is increased, the dynamical ejecta mass increases, while velocity and Y_e decrease, although the trend on the ejecta mass is not statistically significant, given the large inferred numerical uncertainties. This suggests that kN observations could in principle be used to constrain the binary NS mass ratio. Fits to ejecta and disk masses as a function of the mass ratio and the tidal parameter $\tilde{\Lambda}$ will be discussed in a companion paper (V. Nedora et al. 2020, in preparation).

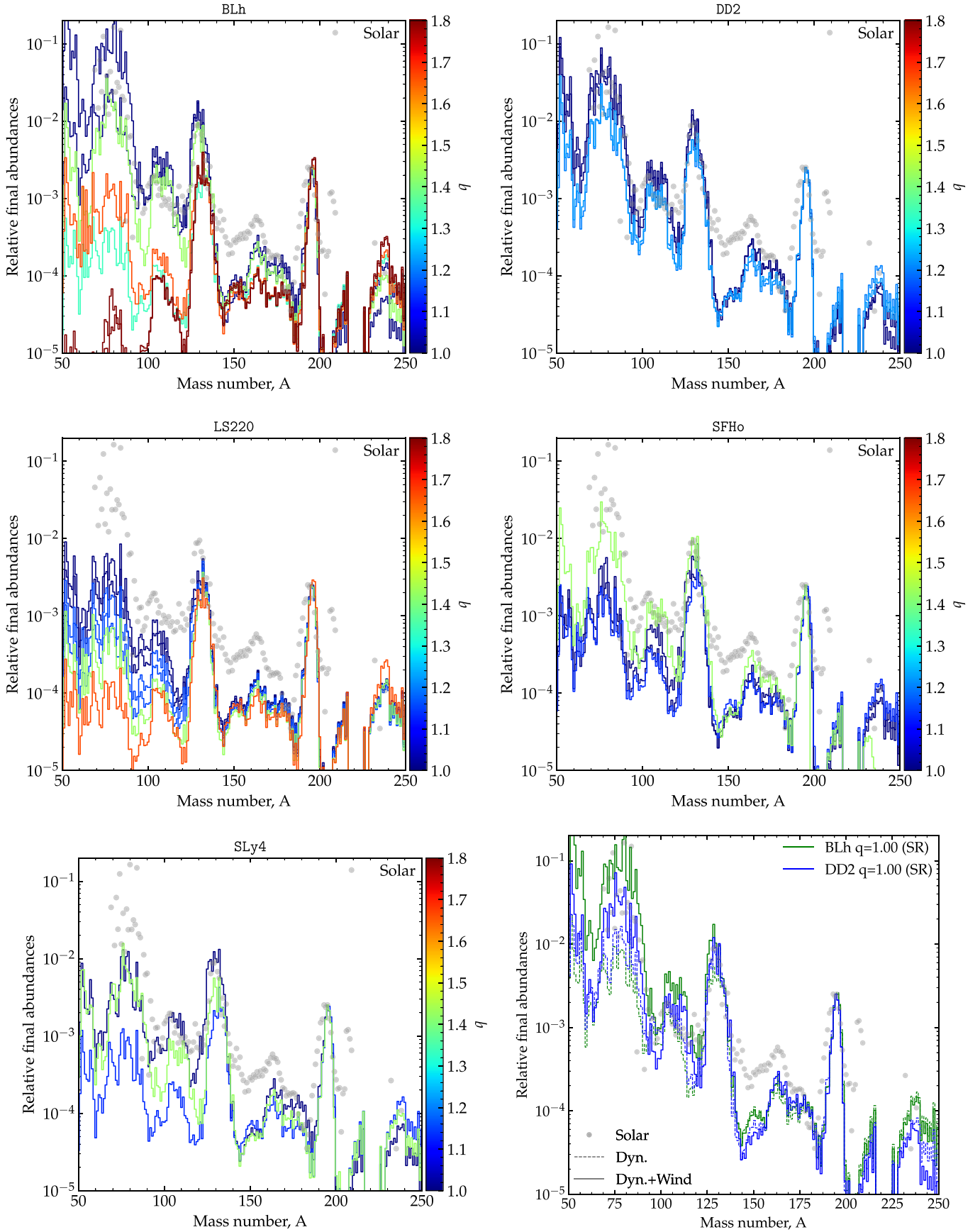


Figure 14. Nucleosynthesis yields for all simulations. Each of the first five panels shows a different EOS, and the color scale shows the dependence on the mass ratio. The nucleosynthesis is computed on the total ejecta computed during the simulations and composed of the dynamical (all models) plus the spiral-wave wind (for the long-lived remnants listed in Table 4). The last (bottom right) panel compares the nucleosynthesis in the dynamical ejecta and spiral-wave wind for the long-lived remnants. The inclusion of the spiral-wave wind contributes to improving the agreement with solar data for elements around the first peak.

If the remnant does not collapse to a BH, the dominant outflow component is found to be the spiral-wave wind (Nedora et al. 2019). This is an outflow driven by spiral density waves that are launched in the disk by the remnant NS as it undergoes the bar-mode and one-armed instabilities (Shibata & Uryu 2000; Paschalidis et al. 2015; Radice et al. 2016a). The spiral-wave wind generates outflows of $\sim 0.1\text{--}0.5 M_{\odot} \text{ s}^{-1}$, which persist for as long as the remnant does not collapse and until the end of our simulations (up to ~ 100 ms). The ejecta have a narrow distribution in velocities with $\langle v_{\infty} \rangle \simeq 0.2 c$ and a broad distribution in Y_e .

At high latitudes, we observed the emergence of a ν -component from the remnants. This high- Y_e outflow component has characteristics that are initially similar to those of the ν -winds reported by, e.g., Dessart et al. (2009), Perego et al. (2014), and Fujibayashi et al. (2020b). However, in our simulations the ν -component is quickly shocked due to the presence of high-density material that is lifted by thermal pressure from the disk and pollutes the polar regions. On the other hand, we remark that previous studies found the emergence of the ν -component only at later times, suggesting that the right conditions for the formation of a steady ν -component might not have been reached in our simulations yet. At the same time, we cannot exclude that the lack of a ν -component arises due to a deficiency in our approximate neutrino treatment. The emergence of the ν -component should be revisited once better neutrino transport schemes are available. It is also important to emphasize that the polar outflow might be strongly magnetized (Siegel & Metzger 2017; Metzger et al. 2018; Fernández et al. 2019; Miller et al. 2019; Mösta et al. 2020). Since our simulations did not include magnetic fields explicitly, we cannot exclude that the properties of these polar outflows will be drastically changed by MHD effects. On the other hand, we remark that a viscous ansatz for angular momentum transport, such as that used here, has been shown to be in good agreement with a full-MHD calculation when considering the properties of the bulk of the secular outflow (Fernández et al. 2019).

We performed nucleosynthesis calculations to analyze the r -process yields in the dynamical ejecta and the spiral-wave wind. We find that, because of the strong dependence of Y_e on q , the yields are sensitive to the binary mass ratio. In particular, very asymmetric binaries produce larger quantities of actinides. Symmetric binaries, instead, tend to produce lighter elements. When the spiral-wave wind is included in the nucleosynthesis calculations, we find that the full solar r -process pattern down to $A \simeq 100$ can be reproduced. However, high-mass-ratio BNS mergers (or BHNS mergers) appear to be required to explain the production of actinides.

None of our simulations produce outflows with properties compatible with those inferred from the direct fitting of simple color light-curve models to AT2017gfo (Villar et al. 2017). However, anisotropic multicomponent kN models informed with our NR data can reproduce some of the key features of AT2017gfo (Perego et al. 2017; Nedora et al. 2019). In particular, the optical emission at 1 day can be explained with a combination of dynamical ejecta and spiral-wave wind from long-lived binaries. However, the rapid collapse of the merger remnant cannot be excluded. For example, Fujibayashi et al. (2020a) found that the kind of high- Y_e material needed to explain the optical data from AT2017gfo might also be produced in winds from BH-torus systems. The infrared

emission from AT2017gfo can only be explained by assuming that $\sim 20\%$ of the remnant disk is unbound by viscous processes and nuclear recombination on a timescale of a few seconds (e.g., Metzger et al. 2008).


Future work should address the limitations of this study. Self-consistent 3D simulations of NS merger systems forming BHs or massive NSs and spanning even longer timescales up to a few seconds are needed to confirm whether or not AT2017gfo can be explained from first principles. Over these timescales, the use of real neutrino transport schemes, such as gray or spectral M1 (Foucart et al. 2016; Roberts et al. 2016), is imperative, since leakage-based schemes, such as our M0 scheme or the M1-leakage scheme of Sekiguchi et al. (2015) and Fujibayashi et al. (2018), cannot correctly treat the diffusion of neutrinos from the interior of the remnant. Finally, the impact of MHD effects in the postmerger still needs to be clarified: they are likely crucial for the launching of jets in NS mergers (Ruiz et al. 2016), but their impact on mass ejection and nucleosynthesis is not as clear (Siegel & Metzger 2018; Fernández et al. 2019).

S.B. and B.D. acknowledge support by the EU H2020 under ERC Starting Grant, no. BinGraSp-714626. Numerical relativity simulations were performed on the supercomputer SuperMUC at the LRZ Munich (Gauss project pn56zo), on supercomputer Marconi at CINECA (ISCRA-B project number HP10BMHFQQ); on the supercomputers Bridges, Comet, and Stampede (NSF XSEDE allocation TG-PHY160025); on NSF/NCSA Blue Waters (NSF AWD-1811236); on ARA cluster at Jena FSU. This research used resources of the National Energy Research Scientific Computing Center, a DOE Office of Science User Facility supported by the Office of Science of the U.S. Department of Energy under Contract No. DE-AC02-05CH11231. Data postprocessing was performed on the Virgo “Tullio” server at Torino supported by INFN. The authors gratefully acknowledge the Gauss Centre for Supercomputing e.V. (www.Gauss-center.eu) for funding this project by providing computing time on the GCS Supercomputer SuperMUC at Leibniz Supercomputing Centre (www.lrz.de).

ORCID iDs

Sebastiano Bernuzzi  <https://orcid.org/0000-0002-2334-0935>

David Radice  <https://orcid.org/0000-0001-6982-1008>

Albino Perego  <https://orcid.org/0000-0002-0936-8237>

Mohammadtaher Safarzadeh  <https://orcid.org/0000-0002-1827-7011>

References

- Abbott, B. P., Abbott, R., Abbott, T. D., et al. 2017a, *ApJL*, **850**, L39
- Abbott, B. P., Abbott, R., Abbott, T. D., et al. 2017b, *PhRvL*, **119**, 141101
- Abbott, B. P., Abbott, R., Abbott, T. D., et al. 2017c, *PhRvL*, **119**, 161101
- Abbott, B. P., Abbott, R., Abbott, T. D., et al. 2018, *PhRvL*, **121**, 161101
- Abbott, B. P., Abbott, R., Abbott, T. D., et al. 2019a, *ApJ*, **875**, 160
- Abbott, B. P., Abbott, R., Abbott, T. D., et al. 2019b, *PhRvX*, **9**, 011001
- Arcavi, I., Hosseinzadeh, G., Howell, D. A., et al. 2017, *Natur*, **551**, 64
- Ardevol-Pulpillo, R., Janka, H. T., Just, O., & Bauswein, A. 2019, *MNRAS*, **485**, 4754
- Argast, D., Samland, M., Thielemann, F., & Qian, Y. 2004, *A&A*, **416**, 997
- Banerjee, P., Wu, M.-R., & Yuan, Z. 2020, *ApJL*, **902**, L34
- Bartos, I., & Marka, S. 2019, *ApJL*, **881**, L4
- Baumgarte, T. W., Shapiro, S. L., & Shibata, M. 2000, *ApJL*, **528**, L29
- Bauswein, A., Goriely, S., & Janka, H.-T. 2013, *ApJ*, **773**, 78

- Beloborodov, A. M. 2008, in AIP Conf. Proc. 1054, Cool discs, hot flows: The Varying Faces of Accreting Compact Objects (Melville, NY: AIP), 51
- Berger, M. J., & Colella, P. 1989, *JCoPh*, **82**, 64
- Berger, M. J., & Olinger, J. 1984, *JCoPh*, **53**, 484
- Bernuzzi, S. 2020, Invited Review for GERG, 2004, 06419
- Bernuzzi, S., Breschi, M., Daszuta, B., et al. 2020, *MNRAS*, **497**, 1488
- Bernuzzi, S., Dietrich, T., & Nagar, A. 2015, *PhRvL*, **115**, 091101
- Bernuzzi, S., Dietrich, T., Tichy, W., & Brügmann, B. 2014, *PhRvD*, **89**, 104021
- Bernuzzi, S., & Hilditch, D. 2010, *PhRvD*, **81**, 084003
- Bernuzzi, S., Nagar, A., Thierfelder, M., & Brügmann, B. 2012, *PhRvD*, **86**, 044030
- Bernuzzi, S., Radice, D., Ott, C. D., et al. 2016, *PhRvD*, **94**, 024023
- Bombaci, I., & Logoteta, D. 2018, *A&A*, **609**, A128
- Bonetti, M., Perego, A., Capelo, P. R., Dotti, M., & Miller, M. C. 2018, *PASA*, **35**, 17
- Bonetti, M., Perego, A., Dotti, M., & Cescutti, G. 2019, *MNRAS*, **490**, 296
- Bovard, L., Martin, D., Guercilena, F., et al. 2017, *PhRvD*, **96**, 124005
- Bramante, J., & Linden, T. 2016, *ApJ*, **826**, 57
- Bruenn, S. W. 1985, *ApJS*, **58**, 771
- Bucciantini, N., Metzger, B., Thompson, T., & Quataert, E. 2012, *MNRAS*, **419**, 1537
- Burrows, A., Reddy, S., & Thompson, T. A. 2006, *NuPhA*, **777**, 356
- Chornock, R., Berger, E., Kasen, D., et al. 2017, *ApJL*, **848**, L19
- Ciolfi, R. 2020, *MNRAS*, **495**, L66
- Côté, B., Eichler, M., Arcones, A., et al. 2019, *ApJ*, **875**, 106
- Coulter, D. A., Foley, R. J., Kilpatrick, C. D., et al. 2017, *Sci*, **358**, 1556
- Cowperthwaite, P. S., Berger, E., Villar, V. A., et al. 2017, *ApJL*, **848**, L17
- Damour, T., Nagar, A., Pollney, D., & Reisswig, C. 2012, *PhRvL*, **108**, 131101
- Danielewicz, P., Lacey, R., & Lynch, W. G. 2002, *Sci*, **298**, 1592
- Danielewicz, P., & Lee, J. 2014, *NuPhA*, **922**, 1
- De, S., Finstad, D., Lattimer, J. M., et al. 2018, *PhRvL*, **121**, 091102 [Erratum: 2018, *PhRvL*, **121**, 259902]
- Dessart, L., Ott, C., Burrows, A., Rosswog, S., & Livne, E. 2009, *ApJ*, **690**, 1681
- Douchin, F., & Haensel, P. 2001, *A&A*, **380**, 151
- Drout, M. R., Piro, A. L., Shappee, B. J., et al. 2017, *Sci*, **358**, 1570
- Duan, H., Friedland, A., McLaughlin, G., & Surman, R. 2011, *JPhG*, **38**, 035201
- East, W. E., Paschalidis, V., & Pretorius, F. 2016a, *CQGrA*, **33**, 244004
- East, W. E., Paschalidis, V., Pretorius, F., & Shapiro, S. L. 2016b, *PhRvD*, **93**, 024011
- Endrizzi, A., Logoteta, D., Giacomazzo, B., et al. 2018, *PhRvD*, **98**, 043015
- Endrizzi, A., Perego, A., Fabbri, F. M., et al. 2020, *EPJA*, **56**, 15
- Evans, P. A., Cenko, S. B., Kennea, J. A., et al. 2017, *Sci*, **358**, 1565
- Fahlman, S., & Fernández, R. 2018, *ApJL*, **869**, L3
- Fernández, R., & Metzger, B. D. 2013, *ApJ*, **763**, 108
- Fernández, R., & Metzger, B. D. 2013, *MNRAS*, **435**, 502
- Fernández, R., & Metzger, B. D. 2016, *ARNPS*, **66**, 23
- Fernández, R., Quataert, E., Schwab, J., Kasen, D., & Rosswog, S. 2015, *MNRAS*, **449**, 390
- Fernández, R., Tchekhovskoy, A., Quataert, E., Foucart, F., & Kasen, D. 2019, *MNRAS*, **482**, 3373
- Foucart, F., Desai, D., Brege, W., et al. 2017, *CQGrA*, **34**, 044002
- Foucart, F., O'Connor, E., Roberts, L., et al. 2016, *PhRvD*, **94**, 123016
- Freiburghaus, C., Rosswog, S., & Thielemann, F.-K. 1999, *ApJL*, **525**, L121
- Fujibayashi, S., Kiuchi, K., Nishimura, N., Sekiguchi, Y., & Shibata, M. 2018, *ApJ*, **860**, 64
- Fujibayashi, S., Sekiguchi, Y., Kiuchi, K., & Shibata, M. 2017, *ApJ*, **846**, 114
- Fujibayashi, S., Shibata, M., Wanajo, S., et al. 2020a, *PhRvD*, **101**, 083029
- Fujibayashi, S., Wanajo, S., Kiuchi, K., et al. 2020b, *PhRvD*, **102**, 123014
- Fuller, G. M., Kusenkov, A., & Takhistov, V. 2017, *PhRvL*, **119**, 061101
- Galeazzi, F., Kastaun, W., Rezzolla, L., & Font, J. A. 2013, *PhRvD*, **88**, 064009
- Gizzi, D., O'Connor, E., Rosswog, S., et al. 2019, *MNRAS*, **490**, 4211
- Goodale, T., Allen, G., Lanfermann, G., et al. 2003, Vector and Parallel Processing—VEPCAR'2002 (Berlin: Springer)
- Gottlieb, S., Ketcheson, D. I., & Shu, C. W. 2009, *JSCoM*, **38**, 251
- Gourgoulhon, E., Grandclement, P., Taniguchi, K., Marck, J.-A., & Bonazzola, S. 2001, *PhRvD*, **63**, 064029
- Hallinan, G., Corsi, A., Mooley, K. P., et al. 2017, *Sci*, **358**, 1579
- Hanauske, M., Takami, K., Bovard, L., et al. 2017, *PhRvD*, **96**, 043004
- Hempel, M., Oertel, M., Typel, S., & Klähn, T. 2017, *JPS Conf. Proc.*, **14**, 010802
- Hempel, M., & Schaffner-Bielich, J. 2010, *NuPhA*, **837**, 210
- Hilditch, D., Bernuzzi, S., Thierfelder, M., et al. 2013, *PhRvD*, **88**, 084057
- Hirai, Y., Ishimaru, Y., Saitoh, T. R., et al. 2015, *ApJ*, **814**, 41
- Hotokozaka, K., Beniamini, P., & Piran, T. 2018, *IJMP*, **D27**, 1842005
- Hotokozaka, K., Kiuchi, K., Kyutoku, K., et al. 2013, *PhRvD*, **88**, 044026
- Janiuk, A. 2019, *ApJ*, **882**, 163
- Ji, A. P., Drout, M. R., & Hansen, T. T. 2019, *ApJ*, **882**, 40
- Ji, A. P., Frebel, A., Chiti, A., & Simon, J. D. 2016, *Natur*, **531**, 610
- Just, O., Bauswein, A., Pulpillo, R. A., Goriely, S., & Janka, H. T. 2015, *MNRAS*, **448**, 541
- Kaplan, J., Ott, C., O'Connor, E., et al. 2014, *ApJ*, **790**, 19
- Kasen, D., Badnell, N. R., & Barnes, J. 2013, *ApJ*, **774**, 25
- Kasliwal, M. M., Nakar, E., Singer, L. P., et al. 2017, *Sci*, **358**, 1559
- Kastaun, W., Cioffi, R., Endrizzi, A., & Giacomazzo, B. 2017, *PhRvD*, **96**, 043019
- Kastaun, W., & Galeazzi, F. 2015, *PhRvD*, **91**, 064027
- Kawaguchi, K., Shibata, M., & Tanaka, M. 2018, *ApJL*, **865**, L21
- Kiuchi, K., Kyutoku, K., Sekiguchi, Y., & Shibata, M. 2018, *PhRvD*, **97**, 124039
- Korobkin, O., Rosswog, S., Arcones, A., & Winteler, C. 2012, *MNRAS*, **426**, 1940
- Korobkin, O., Wollaeger, R., Fryer, C., et al. 2020, arXiv:2004.00102
- Kulkarni, S. R. 2005, *astro-ph/0510256*
- Lattimer, J. M., & Lim, Y. 2013, *ApJ*, **771**, 51
- Lattimer, J. M., & Schramm, D. N. 1974, *ApJL*, **192**, L145
- Lattimer, J. M., & Swesty, F. D. 1991, *NuPhA*, **535**, 331
- Lee, W. H., Ramirez-Ruiz, E., & Diego-Lopez-Camara 2009, *ApJL*, **699**, L93
- Lehner, L., Liebling, S. L., Palenzuela, C., et al. 2016a, *CQGrA*, **33**, 184002
- Lehner, L., Liebling, S. L., Palenzuela, C., & Motl, P. M. 2016b, *PhRvD*, **94**, 043003
- Li, L.-X., & Paczynski, B. 1998, *ApJL*, **507**, L59
- Lippuner, J., Fernández, R., Roberts, L. F., et al. 2017, *MNRAS*, **472**, 904
- Lippuner, J., & Roberts, L. F. 2015, *ApJ*, **815**, 82
- Löffler, F., Faber, J., Bentivegna, E., et al. 2012, *CQGrA*, **29**, 115001
- Logoteta, D., Bombaci, I., & Kievsky, A. 2016, *PhRvC*, **94**, 064001
- Lyman, J. D., Lamb, G. P., Levan, A. J., et al. 2018, *NatAs*, **2**, 751
- Machleidt, R., & Entem, D. R. 2011, *PhR*, **503**, 1
- Martin, D., Perego, A., Arcones, A., et al. 2015, *ApJ*, **813**, 2
- Metzger, B., Martinez-Pinedo, G., Darbha, S., et al. 2010, *MNRAS*, **406**, 2650
- Metzger, B., Piro, A., & Quataert, E. 2008, *MNRAS*, **390**, 781
- Metzger, B. D., & Fernández, R. 2014, *MNRAS*, **441**, 3444
- Metzger, B. D., Thompson, T. A., & Quataert, E. 2007, *ApJ*, **659**, 561
- Metzger, B. D., Thompson, T. A., & Quataert, E. 2018, *ApJ*, **856**, 101
- Miller, J. M., Ryan, B. R., Dolence, J. C., et al. 2019, *PhRvD*, **100**, 023008
- Mooley, K. P., Deller, A. T., Gottlieb, O., et al. 2018, *Natur*, **561**, 355
- Mösta, P., Radice, D., Haas, R., Schnetter, E., & Bernuzzi, S. 2020, *ApJL*, **901**, L37
- Mösta, P., Roberts, L. F., Halevi, G., et al. 2018, *ApJ*, **864**, 171
- Nedora, V., Bernuzzi, S., Radice, D., et al. 2019, *ApJL*, **886**, L30
- Neilsen, D., Liebling, S. L., Anderson, M., et al. 2014, *PhRvD*, **89**, 104029
- Nicholl, M., Berger, E., Kasen, D., et al. 2017, *ApJL*, **848**, L18
- Nishimura, N., Sawai, H., Takiwaki, T., Yamada, S., & Thielemann, F.-K. 2017, *ApJL*, **836**, L21
- Nishimura, N., Takiwaki, T., & Thielemann, F. K. 2015, *ApJ*, **810**, 109
- O'Connor, E., & Ott, C. D. 2010, *CQGrA*, **27**, 114103
- Oechslin, R., Janka, H.-T., & Marek, A. 2006, *A&A*, arXiv:astro-ph/0611047
- Palenzuela, C., Liebling, S. L., Neilsen, D., et al. 2015, *PhRvD*, **92**, 044045
- Paschalidis, V., East, W. E., Pretorius, F., & Shapiro, S. L. 2015, *PhRvD*, **92**, 121502
- Perego, A., Bernuzzi, S., & Radice, D. 2019, *EPJA*, **55**, 124
- Perego, A., Cabezon, R., & Kaeppli, R. 2016, *ApJS*, **223**, 22
- Perego, A., Radice, D., & Bernuzzi, S. 2017, *ApJL*, **850**, L37
- Perego, A., Rosswog, S., Cabezon, R., et al. 2014, *MNRAS*, **443**, 3134
- Piarulli, M., Girlanda, L., Schiavilla, R., et al. 2016, *PhRv*, **C94**, 054007
- Pollney, D., Reisswig, C., Schnetter, E., Dorband, N., & Diener, P. 2011, *PhRvD*, **83**, 044045
- Prantzos, N., Abia, C., Cristallo, S., Limongi, M., & Chieffi, A. 2020, *MNRAS*, **491**, 1832
- Pritychenko, B. 2019, arXiv:1905.06165
- Qian, Y., & Woosley, S. 1996, *ApJ*, **471**, 331
- Radice, D. 2017, *ApJL*, **838**, L2
- Radice, D. 2020, arXiv:2005.09002
- Radice, D., Bernuzzi, S., Del Pozzo, W., Roberts, L. F., & Ott, C. D. 2017, *ApJL*, **842**, L10
- Radice, D., Bernuzzi, S., & Ott, C. D. 2016a, *PhRvD*, **94**, 064011
- Radice, D., Bernuzzi, S., & Perego, A. 2020, *ARNPS*, **70**, 95
- Radice, D., Galeazzi, F., Lippuner, J., et al. 2016b, *MNRAS*, **460**, 3255
- Radice, D., Perego, A., Bernuzzi, S., & Zhang, B. 2018a, *MNRAS*, **481**, 3670

- Radice, D., Perego, A., Hotokezaka, K., et al. 2018b, [ApJ](#), **869**, 130
- Radice, D., Perego, A., Zappa, F., & Bernuzzi, S. 2018c, [ApJL](#), **852**, L29
- Radice, D., & Rezzolla, L. 2012, [A&A](#), **547**, A26
- Radice, D., Rezzolla, L., & Galeazzi, F. 2014a, [MNRAS](#), **437**, L46
- Radice, D., Rezzolla, L., & Galeazzi, F. 2014b, [CQGrA](#), **31**, 075012
- Reisswig, C., Haas, R., Ott, C. D., et al. 2013a, [PhRvD](#), **87**, 064023
- Reisswig, C., Ott, C., Abdikamalov, E., et al. 2013b, [PhRvL](#), **111**, 151101
- Roberts, L. F., Kasen, D., Lee, W. H., & Ramirez-Ruiz, E. 2011, [ApJL](#), **736**, L21
- Roberts, L. F., Ott, C. D., Haas, R., et al. 2016, [ApJ](#), **831**, 98
- Rosswog, S. 2005, [ApJ](#), **634**, 1202
- Rosswog, S., & Davies, M. B. 2003, [MNRAS](#), **345**, 1077
- Rosswog, S., Korobkin, O., Arcones, A., Thielemann, F. K., & Piran, T. 2014, [MNRAS](#), **439**, 744
- Rosswog, S., & Liebendoerfer, M. 2003, [MNRAS](#), **342**, 673
- Rosswog, S., Liebendoerfer, M., Thielemann, F., et al. 1999, [A&A](#), **341**, 499
- Rosswog, S., & Ramirez-Ruiz, E. 2003, [MNRAS](#), **343**, L36
- Rosswog, S., Ramirez-Ruiz, E., & Davies, M. B. 2003, [MNRAS](#), **345**, 1077
- Ruan, J. J., Nynka, M., Haggard, D., Kalogera, V., & Evans, P. 2018, [ApJL](#), **853**, L4
- Ruffert, M., Janka, H., Takahashi, K., & Schäfer, G. 1997, [A&A](#), **319**, 122
- Ruffert, M. H., Janka, H. T., & Schäfer, G. 1996, [A&A](#), **311**, 532
- Ruiz, M., Lang, R. N., Paschalidis, V., & Shapiro, S. L. 2016, [ApJL](#), **824**, L6
- Safarzadeh, M., & Côté, B. 2017, [MNRAS](#), **471**, 4488
- Safarzadeh, M., Ramirez-Ruiz, E., Andrews, J. J., et al. 2019a, [ApJ](#), **872**, 105
- Safarzadeh, M., Sarmiento, R., & Scannapieco, E. 2019b, [ApJ](#), **876**, 28
- Schneider, A. S., Roberts, L. F., & Ott, C. D. 2017, [PhRvC](#), **96**, 065802
- Schnetter, E., Hawley, S. H., & Hawke, I. 2004, [CQGrA](#), **21**, 1465
- Schnetter, E., Ott, C. D., Allen, G., et al. 2007, [arXiv:0707.1607](#)
- Sekiguchi, Y. 2010, [PTHPh](#), **124**, 331
- Sekiguchi, Y., Kiuchi, K., Kyutoku, K., & Shibata, M. 2011, [PhRvL](#), **107**, 051102
- Sekiguchi, Y., Kiuchi, K., Kyutoku, K., & Shibata, M. 2015, [PhRvD](#), **91**, 064059
- Sekiguchi, Y., Kiuchi, K., Kyutoku, K., Shibata, M., & Taniguchi, K. 2016, [PhRvD](#), **93**, 124046
- Shapiro, S. L., & Teukolsky, S. A. 1983, *Black Holes, White Dwarfs, and Neutron Stars: The Physics of Compact Objects* (New York: Wiley)
- Shibata, M., & Taniguchi, K. 2006, [PhRvD](#), **73**, 064027
- Shibata, M., Taniguchi, K., & Uryu, K. 2005, [PhRvD](#), **71**, 084021
- Shibata, M., & Uryu, K. 2000, [PhRvD](#), **61**, 064001
- Siegel, D. M. 2019, [EPJA](#), **55**, 203
- Siegel, D. M., Barnes, J., & Metzger, B. D. 2019, [Natur](#), **569**, 241
- Siegel, D. M., & Metzger, B. D. 2017, [PhRvL](#), **119**, 231102
- Siegel, D. M., & Metzger, B. D. 2018, [ApJ](#), **858**, 52
- Skúladóttir, A., Hansen, C. J., Salvadori, S., & Choplin, A. 2019, [A&A](#), **631**, A171
- Smartt, S. J., Chen, T. W., Jerkstrand, A., et al. 2017, [Natur](#), **551**, 75
- Soares-Santos, M., Holz, D. E., Annis, J., et al. 2017, [ApJL](#), **848**, L16
- Steiner, A. W., Hempel, M., & Fischer, T. 2013a, [ApJ](#), **774**, 17
- Steiner, A. W., Lattimer, J. M., & Brown, E. F. 2013b, [ApJL](#), **765**, L5
- Symbalisty, E., & Schramm, D. N. 1982, [ApL](#), **22**, 143
- Tanaka, M., Utsumi, Y., Mazzali, P. A., et al. 2017, [PASJ](#), **69**, 102
- Tanvir, N. R., Levan, A. J., González-Fernández, C., et al. 2017, [ApJL](#), **848**, L27
- Troja, E., Piro, L., van Eerten, H., et al. 2017, [Natur](#), **551**, 71
- Typel, S., Ropke, G., Klahn, T., Blaschke, D., & Wolter, H. H. 2010, [PhRv](#), **C81**, 015803
- van de Voort, F., Pakmor, R., Grand, R. J., et al. 2020, [MNRAS](#), **494**, 4867
- van Riper, K., & Lattimer, J. 1981, [ApJ](#), **249**, 270
- Vassh, N., Mumpower, M. R., McLaughlin, G. C., Sprouse, T. M., & Surman, R. 2020, [ApJ](#), **896**, 28
- Villar, V. A., Guillochon, J., Berger, E., et al. 2017, [ApJL](#), **851**, L21
- Vincent, T., Foucart, F., Duez, M. D., et al. 2020, [PhRvD](#), **101**, 044053
- Wanajo, S., Sekiguchi, Y., Nishimura, N., et al. 2014, [ApJL](#), **789**, L39
- Wehmeyer, B., Frohlich, C., Côté, B., Pignatari, M., & Thielemann, F.-K. 2019, [MNRAS](#), **487**, 1745
- Winteler, C., Kaeppli, R., Perego, A., et al. 2012, [ApJL](#), **750**, L22
- Wu, M.-R., Fernández, R., Martínez-Pinedo, G., & Metzger, B. D. 2016, [MNRAS](#), **463**, 2323
- Zappa, F., Bernuzzi, S., Radice, D., Perego, A., & Dietrich, T. 2018, [PhRvL](#), **120**, 111101